ZAŁĄCZNIK 5

GŁÓWNE OSIĄGNIĘCIE NAUKOWE - PUBLIKACJE

SCIENTIFIC REPORTS

OPEN

Visualization of the internal structure of *Didymosphenia geminata* frustules using nano X-ray tomography

Received: 9 January 2017
Accepted: 20 July 2017
Published online: 22 August 2017

Izabela Zgłobicka[1], Qiong Li[2,3], Jürgen Gluch[2], Magdalena Płocińska[1], Teresa Noga[4], Romuald Dobosz[1], Robert Szoszkiewicz[1,5], Andrzej Witkowski[6], Ehrenfried Zschech[2,3] & Krzysztof J. Kurzydłowski[7]

For the first time, the three-dimensional (3D) internal structure of naturally produced *Didymosphenia geminata* frustules were nondestructively visualized at sub-100 nm resolution. The well-optimized hierarchical structures of these natural organisms provide insight that is needed to design novel, environmentally friendly functional materials. Diatoms, which are widely distributed in freshwater, seawater and wet soils, are well known for their intricate, siliceous cell walls called 'frustules'. Each type of diatom has a specific morphology with various pores, ribs, minute spines, marginal ridges and elevations. In this paper, the visualization is performed using nondestructive nano X-ray computed tomography (nano-XCT). Arbitrary cross-sections through the frustules, which can be extracted from the nano-XCT 3D data set for each direction, are validated via the destructive focused ion beam (FIB) cross-sectioning of regions of interest (ROIs) and subsequent observation by scanning electron microscopy (SEM). These 3D data are essential for understanding the functionality and potential applications of diatom cells.

Diatoms (Bacillarophyceae) are unicellular, eukaryotic and photoautotrophic organisms that inhabit aquatic and terrestrial environments. An estimate of diatom diversity ranges from 100,000 to 200,000 species[1–3]. Diatoms are characterized by the presence of a siliceous cell wall called a 'frustule'. The size of a single diatom frustule ranges between 1 µm and 5.6 mm[4–6]. The species from the lowermost region of the spectrum can range from 1 µm to a couple of dozen micrometres (e.g. Li *et al.*, 2016)[7]. Likewise, the species from the largest part of the size spectrum can exceed 5 mm at the maximum but are never smaller than ca. 0.8–1.0 mm. Despite a broad size range of the siliceous exoskeleton in diatom cells, their ultrastructural elements (ornamentation) possess a strict pattern and quantitative measure. Morphometric characters, where characters are described in proportion to the cell size, such as the density of ribs, stria, or pores in 10 µm, or mathematical descriptions of the pore shape have become more common in diatom identification. These morphometric characters have been shown to be species specific and genetically controlled[8]. Therefore, if the measurements are performed on cells across the size range, these patterns of ornamentation remain the same. For example, the stria density in 10 µm will remain within the same range in a species, regardless of cell size.

The diatom frustule is mainly composed of biogenic opaline silica and either organic polymers[9] or chitin[10]. The frustule comprises two overlapping valves with a few to many girdle bands that enclose the protoplast[11–15].

[1]Faculty of Materials Science and Engineering, Warsaw University of Technology, 141 Wołoska Str., 02–507, Warsaw, Poland. [2]Fraunhofer–Institut für Keramische Technologien und Systeme IKTS, Maria–Reiche–Strasse 2, 01109, Dresden, Germany. [3]Dresden Center for Nanoanalysis, Technische Universität Dresden, 10 Helmholtzstraße, 01069, Dresden, Germany. [4]Faculty of Biology and Agriculture, University of Rzeszów, 1 Ćwiklińskiej Str., 35–601, Rzeszów, Poland. [5]Faculty of Chemistry, University of Warsaw, 1 Pasteura Str., 02–093, Warsaw, Poland. [6]Faculty of Geosciences, Paleoceanology Unit, Natural Science Research and Educational Center, University of Szczecin, 18 Mickiewicza Str., 70–383, Szczecin, Poland. [7]Faculty of Mechanical Engineering, Bialystok University of Technology, 45C Wiejska Str., 15–351, Bialystok, Poland. Correspondence and requests for materials should be addressed to I.Z. (email: izabela.zglobicka@inmat.pw.edu.pl)

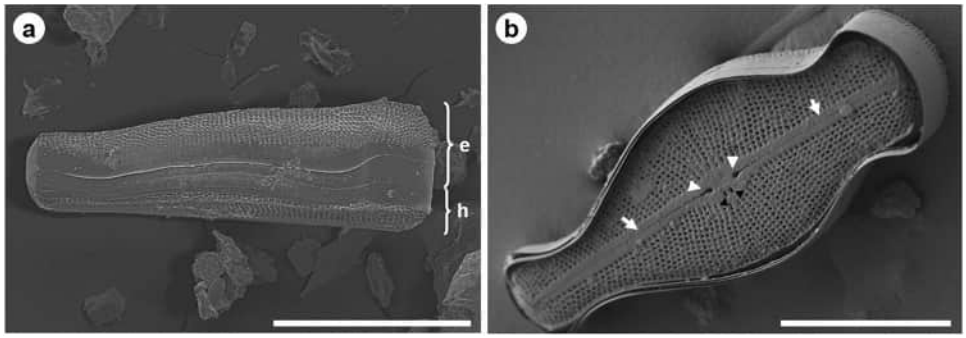

Figure 1. SEM images of *D. geminata* frustule: (**a**) girdle view (e – epivalve, h – hypovalve); (**b**) valve view. Note the presence of the apically oriented slit (*arrows*). The raphe was composed of two branches and two expanded pores. The external central raphe endings mark the extent of the central nodule (*white arrowheads*). The two closely located pores represent an opening of the stigmata (*black arrowheads*). Scale bars: 40 µm (**a**,**b**).

On the basis of the frustule symmetry, diatoms are divided into two major groups: centrics (with either radial or bilateral symmetry) and pennates (with bilateral symmetry)[6,12,13].

The diatom frustule, because of its overall shape and the presence of specific internal substructures (e.g. linking spines, long processes and setae), provides a protective role against grazers and predators[16]. Measurements of the elastic modulus and hardness of silica using nanoindentation have shown a variation in these material parameters that depends upon the location within the frustule[17,18]. Likewise, the size of the diatom frustule influences its fracture resistance. Generally, a smaller cell size requires greater mechanical strength to break the frustule[19]. These mechanical properties appear to be the result of the frustule's hierarchical architecture, particularly the presence of ribs or pores/areoles, which can dissipate the mechanical stress to the entire frustule. These particular mechanical properties originate from the unique and intricate microstructural and nanostructural design of the frustule[17,20–22].

The growing interest in studies of the siliceous component of diatoms has been stimulated by a large variety of applications ranging from those that take advantage of mechanical properties[19] to medicine[23,24], electronics[25] and biomimetics[6,26]. These applications require knowledge of the internal structure of diatoms, which can be obtained via nondestructive high-resolution 3D imaging, so that the natural size, orientation and proximity of the cell components can be determined. Both nano X–ray tomography and focused ion beam (FIB)-based serial cutting techniques with subsequent imaging by scanning electron microscopy (SEM) are options to provide 3D information about the internal structure of diatom frustules. The main difference between these two techniques is that FIB–SEM is a destructive technique, whereas nano-XCT is a nondestructive technique. Furthermore, the slicing direction with FIB–SEM is limited, which causes a lack of options with regard to intersecting the entire diatom frustule (along the long axis). Problems with FIB–SEM reconstructions have been encountered with porous materials (like diatoms) because of excessive brightness and the so-called edge effect of SEM[27], where electrons are more easily excited from the edge of a solid feature. The solution to this problem is pore impregnation with epoxy. The impregnation material must be properly matched with chemical composition, pore size, and fragility of the tested material. With nano-XCT, however, the contrast is achieved without additional preparation processes. An important fact is that FIB–SEM must be conducted in vacuum, whereas nano-XCT, which is conducted at multi-keV photon energies, does not require vacuum conditions.

This paper presents a novel approach for the high-resolution imaging of internal structures of diatom frustules via nano X-ray computed tomography (nano-XCT) complemented by SEM imaging of FIB cross-sections through the ROI, to nondestructively study diatoms and their biomineralization kinetics.

Results and Discussion

The visualization of the diatom frustule was conducted on *Didymosphenia geminata*, a biraphid pennate diatom. SEM images (Fig. 1) illustrate girdle (A) and valve (B) views of the *D. geminata* frustule. The images clearly show that one of the valves, the epivalve (Fig. 1a, marked with 'e') is larger than the other one, the hypovalve (Fig. 1a, marked with 'h'). Nano-XCT studies of the frustules of *D. geminata* show both surface and internal structures of the frustules in a nondestructive manner based on a single tomographic data set. Figure 2a shows the entire frustule of *D. geminata* in one projection (exposure time of 180 s) as an arbitrary cross-section. From the 3D tomographic imaging, the radiograph shows all surface and internal structures; more details are distinguishable in individual cross-sections based on nano-XCT. Both X-ray and SEM images provide information regarding the geometry of the *D. geminata* frustule.

Measurements of the *D. geminata* frustule (including the length of the entire frustule; the greatest thickness at the head pole, central region and foot pole; and the distance between stigmata) are indicated in Fig. 3 and listed in Table 1. On the basis of these results, the frustule shows considerable asymmetry along the apical axis, which is expressed by the variations in the width of the frustule ends (apices) and the position of the centre of gravity.

According to Dawson (1973) and Moffat (1994), *D. geminata* valves are relatively large compared with those of other diatoms; the valves are 120–140 µm in length and 35–45 µm in width[28,29]. However, Spaulding (2010) claims a much larger size range for the valves of *D. geminata*: from 65 µm to 161 µm in length and from 36 µm to 41 µm in width[30]. On the basis of SEM images (n = 24) of the frustules, we calculated an average length (A) and width (C)

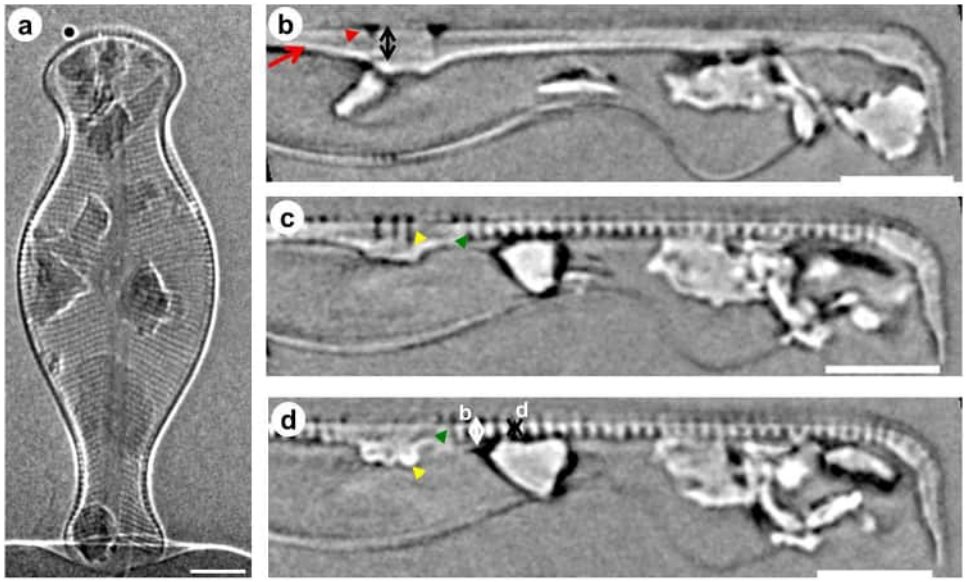

Figure 2. Nano–XCT results of the frustule of *D. geminata*. (**a**) One projection of the entire frustule of *D. geminata* imaged by nano–XCT in phase contrast mode. (**b**–**d**) One slice extracted from the reconstructed 3D volume in girdle view of the frustule. *Red arrowheads*: raphe, *red arrow*: raphe extending, *green arrowheads*: ribs, *yellow arrowheads*: stigmata, *white and double arrows*: width, height, and distance of the ribs and struts. Scale bars: 10 µm (**a**–**d**).

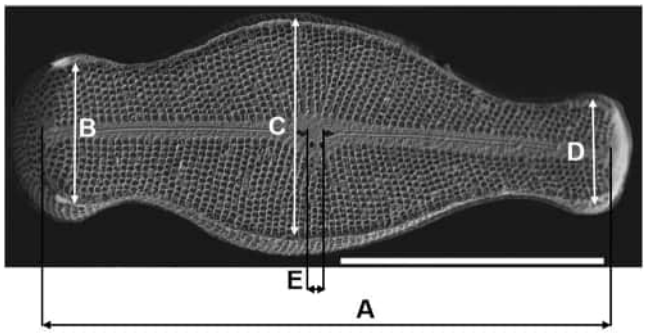

Figure 3. SEM image of the *D. geminata* frustule with marked size dimensions: *A* – apical axis of the frustule; *B* through *D* – transapical axis. Scale bar: 40 µm.

Imaging method	Length (A) [µm]	Width, head pole (B) [µm]	Width, middle part (C) [µm]	Width, foot pole (D) [µm]	Distance between proximal ends (E) [µm]
SEM	86.7 ± 8.2	19.8 ± 2.1	30.9 ± 3.1	13.6 ± 1.6	4.9 ± 0.7
Nano–XCT	89.1	24.7	35.8	18.1	4.5

Table 1. The mean values with standard deviations of *D. geminata* size dimensions (according to the designation in Figs 2–4).

of 87 ± 8 µm (A) and 31 ± 3 µm (C), respectively, for a single cell of *D. geminata*. These results suggest that these data originating from this study are smaller than the literature data. Specifically, our results show that the apical end (B) is approximately 1.5 times wider than the distal end (D) (Table 1).

Each valve of *D. geminata* has two raphe branches that are both slits through the valve. According to Moffat (1994) and Aboal *et al*. (2012), in the central region of the valve, 3–6 stigmata are observed and are placed unilaterally near the external proximal ends of the raphe[29,31]. Notably, the nano-XCT and SEM data (see Table 1E) show that the distance between the two central external raphe endings (red arrowhead in Fig. 4a) in this frustule ranges from 4.2 to 5.6 µm. Additionally, the depth of the openings of the external central raphe endings was measured (black double arrow in Fig. 2b) and shown to be approximately 3.6 µm (Table 2A). Each external proximal raphe end forms a cone in the centre of the frustule and extends towards the apices. During our investigations,

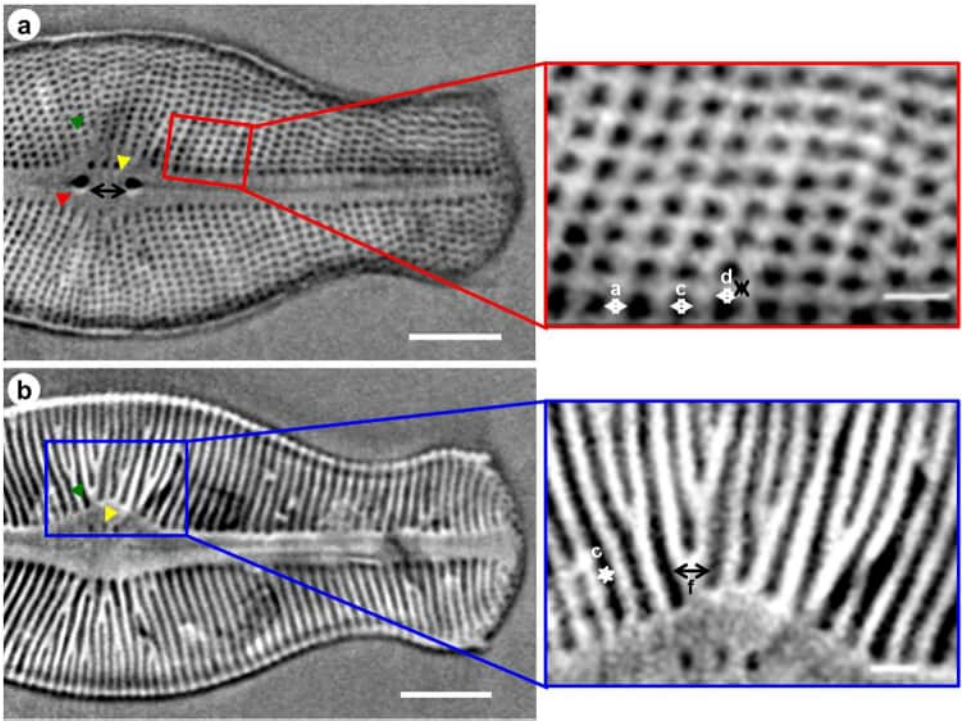

Figure 4. (**a**,**b**) Nano-XCT results of the valve view of the frustule of *D. geminata* from the surface to the valve interior in the Z direction (one slice extracted from the reconstructed 3D volume). Insets: zoomed regions of (**a**) (*red rectangle*) and (**b**) (*blue rectangle*). *Red arrowheads*: raphe, *green arrowheads*: ribs, *yellow arrowheads*: stigmas, *white* and *double arrows*: width, height, and distance of the ribs and struts. Scale bars: 10 µm (**a**,**b**); 2 µm (insets).

Imaging method	Depth of central raphe ending (A) [µm]	Width of stigma (B) [µm]	Depth of stigma (C) [µm]
Nano-XCT	3.58 ± 0.05	0.69 ± 0.065	1.59 ± 0.26

Table 2. Average values with standard deviations of other parameters of the *D. geminata* cell structure from the nano-XCT tomography data set (marked in Figs 2 and 4).

the frustules of *D. geminata* possessed two or three stigmata (yellow arrowheads in Figs 2c,d and 4b,c), which are localized near the proximal raphe ending with a width of 0.7 µm and a depth of 1.6 µm (Table 2B and C). Stigmata appear as isolated pores (Fig. 4a,b) in the valve view and open internally with a complex morphology that is resolved in the girdle view (Fig. 2c,d).

Images of the internal surface of the frustule, which were obtained using the FIB–SEM technique (Fig. 5), show that the major structural features are ribs that extend from the centre of the valve towards the girdle. These structures and the interior of the frustule are specifically depicted using nano-XCT (Figs 2b–d and 4). Note that a substantial portion of each rib is forked to compensate for the difference in the dimensions along the outer and inner edges. More details of the ribs are shown in Fig. 6.

The width (0.58 ± 0.03 µm), height (1.25 ± 0.15 µm) and the distances between ribs (1.05 ± 0.07 µm) and struts (0.49 ± 0.04 µm) of the rib sections were determined from SEM images of frustule cuts (see Table 3). The dimensions of the ribs of the frustules were also measured via nano-XCT (see Figs 2d and 4 (insets) and Table 3). The width of a single rib (a) is, on average, 0.5 µm; the distance between the ribs (c) is 1.1 µm; the depth (height) of the rib (b) is 1.1 µm; and the width and height of the strut are 0.5 µm and 0.3 µm, respectively.

To more specifically show the distance between the ribs and find the regular distribution law of the ribs, the distances between ribs at various positions in the valve view in the Z direction were calculated. Thus, positions 1, 2, 3, and 4 were chosen for the central region and positions 5 and 6 were chosen for the part of the foot pole (head pole). From the measurements of the distance between ribs at these positions at both sides, a curve was plotted, as shown in Fig. 7b. Positions 1–4 in Fig. 7b show a regular pattern in the central region, in which the distance of ribs decreased at a position far from the symmetry axis (apical axis). Additionally, the rib distance from positions 5 and 6 in the part of the head pole. follows the same rule. Because *D. geminata* is a pennate diatom and the ribs are symmetrical about the apical axis along the raphe slit, the other side B also follows this rule (Fig. 7b). Moreover, the width of the ribs in the central region are much larger than that in other regions, with a maximum rib width (Figs 2, 4 and 7) of approximately 1.4 µm. This observation is in agreement with our expectation that the rib's

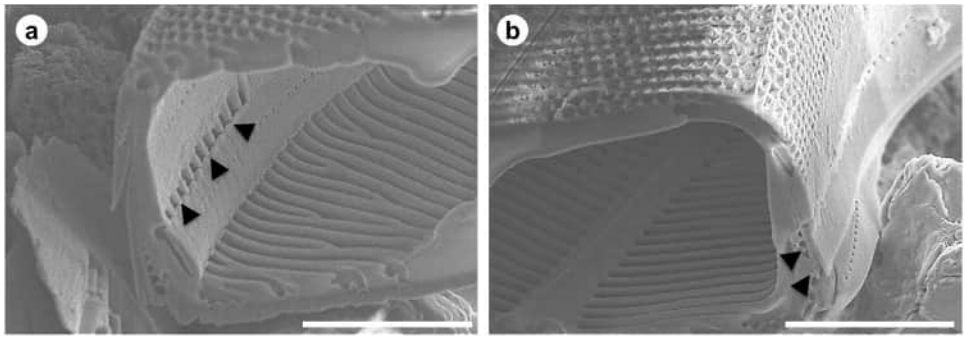

Figure 5. SEM image of an FIB cross-section through the *D. geminata* frustule, showing an overlapping epivalve and interlocking of adjacent girdle bands (marked with arrows): (**a**) left side, (**b**) right side. Scale bars: 10 µm.

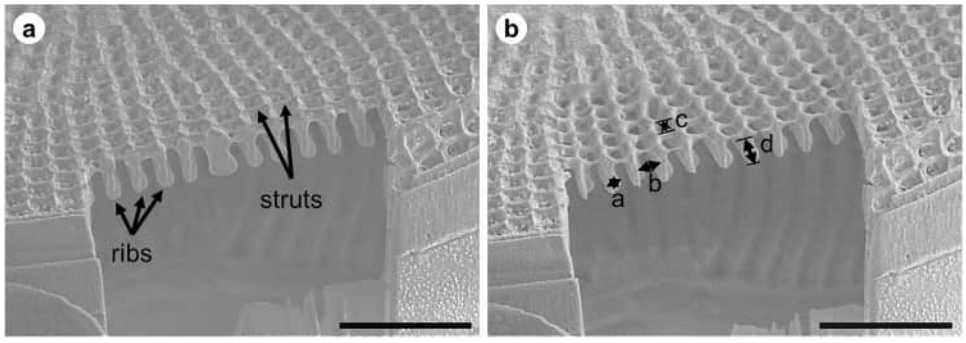

Figure 6. (**a**) SEM images of an FIB cross-section of the *D. geminata* frustule showing internal ribs. (**b**) The cross-section after further cuts with marked dimensions. Scale bars: 5 µm.

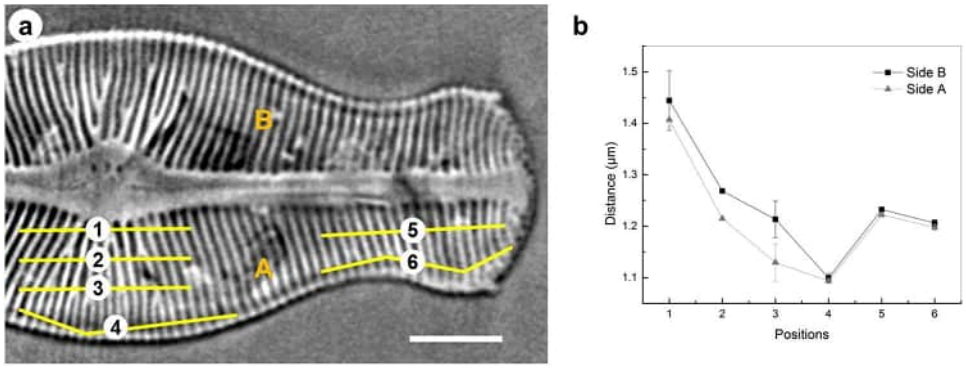

Figure 7. (**a**) The measurement of the rib distance at several positions (from 1 to 6) in the valve view of the *D. geminata* frustule. (**b**) Statistics of the distance between the ribs from centre to centre and from the centre area to the edge area of the *D. geminata* frustule. Scale bar: 10 µm.

Imaging method	Width [µm]	Height [µm]	Distance between ribs [µm]	Gap between struts [µm]
SEM	0.58 ± 0.03	1.25 ± 0.15	1.05 ± 0.07	0.49 ± 0.04
Nano-XCT	0.53 ± 0.10	1.10 ± 0.14	1.09 ± 0.01*	0.50 ± 0.09

Table 3. Average dimensions with standard deviations of the ribs of the *D. geminata* cell structure marked in Figs 2, 4 and 6. *The distance between ribs is position 4 in Fig. 7.

distance in this region is larger than in other regions. The morphology of the ribs in the centre region is similar to that of the limb of a tree that extends to several branches (ribs).

The transapically oriented ribs are interconnected with short apically oriented struts, which contribute to the development of the areolae (pore-like) pattern on the external surface, which is much smoother than the internal one because of the architecture.

In summary, the entire 3D data set of the frustule that was determined using nano-XCT provides detailed morphological information, not only from the surface but also from the valve interior. The detailed 3D structure provides a complete nondestructive 3D view, which provides a basis for further modelling of the diatom structure.

Conclusions

A detailed study of internal structures of *D. geminata* frustules using advanced high-resolution imaging is reported in this paper. The nano-XCT-measured 3D data (Tables 1 and 3) from a single frustule were determined at different positions. These data are not exactly the same as observations made using SEM, which were acquired from different frustules. The subtle differences between these measurements based on nano-XCT and SEM result from the variation in size of the diatom frustules, even in cases where the measured specimens represent the same species. Note that we did not use the identical frustule for imaging with both techniques.

Nano-XCT provides access to additional dimensions, e.g. the depth of the raphe (Fig. 2b) and depth of the stigma (Fig. 2c,d). Because the tomographic data set allows arbitrary cross-sections to be taken through any region of the frustule, measurement of, for example, the distance between the ribs at various locations (Fig. 7) becomes possible.

To summarize, nano-XCT provides a nondestructive high-resolution 3D data set of the diatom structure with detailed morphological information. This detailed 3D structural information from nano-XCT, which is based on arbitrary cross-sections through the diatom, provides novel information regarding the diatom substructure. The 3D data based on nano-XCT were validated via SEM images of FIB cross-sections through the ROI, and the dimensions of diatom substructures based on tomographic data were confirmed. The 3D information of the diatom substructures enables the validation and improvement of models related to mechanical parameters such as strength and stiffness.

Experimental Materials and Methods

Materials. The *D. geminata* studied in this paper was sampled in the Wisłoka River, Krempna Village, Subcarpathian Province in SE Poland. The expedition was conducted in July 2013. The following environmental conditions were measured during the sampling: pH = 7.9, conductivity = 276 μS cm^{-1}, and water temperature = 21.0 °C. The water contained 2.95 mg L^{-1} of chlorides, 0.12 mg L^{-1} of nitrates, and 16.7 mg L^{-1} of sulphates. *D. geminata* samples were carefully scraped from boulders located inside the riverbed using a scrub brush with synthetic bristles. The fresh samples were immediately transported in special plastic boxes with riverine water to the laboratory (Warsaw University of Technology) for further study. In the laboratory, the cells were separated from the stalks. The scraped material was inserted into nylon-mesh filtration bags (Carl–Roth, GmbH, Germany) and immersed in distilled water for dialysis to remove dissolved salts from the natural stream waters. The dialysed material was then sonicated for 12 h using a CD-4860 digital ultrasonic cleaner (Xiejian, Guangdong, China) in continuous mode without heating. The cells collected from the tube were boiled in 37% hydrogen peroxide (H_2O_2) to remove organic matter. The final suspension was washed several times with distilled water and dried in a vacuum dryer at 37 °C for 12 h.

Experimental techniques. *Scanning electron microscopy of diatom frustules.* The frustules of *D. geminata* from the water suspension were spread over a double-sided adhesive carbon tape on an aluminium pin disc using a pipette. For imaging at highest resolution via field-emission scanning electron microscopy (FE-SEM), samples were coated with Au/Pd (7 nm layer) using a high-vacuum sputter coater (Leica EM SCD500, Germany). Cross-sectioning and imaging were carried out with a dual-beam FIB–SEM tool (Hitachi NB5000, Japan) using acceleration voltages of 3.0 kV to 5.0 kV for the electrons.

Nano X–ray computed tomography (nano-XCT) of diatom frustules. A Nano-XCT tool (Xradia nano-XCT-100, US) was used in Zernike phase contrast imaging mode to image the frustules of *D. geminata*[32]. The detailed experimental setup of the nano-XCT tool is described in Li *et al.* (2016)[33]. The isolated and dried frustule *of D. geminata* was mounted on the top of a needle and a gold fiducial marker was carefully positioned on top of the sample for the alignment of the individual images acquired at several tilt angles for tomographic reconstruction. The complete tomographic data set comprised 401 images, which were collected over 180° with an exposure time of 160 s for each individual image. These images were aligned using a custom plugin in ImageJ[34] and subsequently reconstructed using the Xradia Inc. commercial software package[32].

References

1. Armbrust, E. The life of diatoms in the world's oceans. *Nature* **459**, 185–192 (2009).
2. Fourtanier, E. & Kociolek, J. Catalogue of diatom names [online]. Available at: http://research.calacademy.org/izg/research/diatom (2013).
3. Mann, D. G. & Vanormelingen, P. An inordinate fondness? the number, distributions, and origins of diatom species. *Journal of Eukaryotic Microbiology* **60**, 414–420 (2013).
4. Hasle, G. & Syvertsen, E. In *Identifying Marine Diatoms and Dinoflagellates* (ed. Tomas, C.) 5–385 (Academic Press Inc., 1996).
5. Chiovitti, A., Dougdale, T. & Wetherbee, R. In *Biological Adhesives* (eds Smith, A. & Callow, J.) **1** (2006).
6. Gordon, R., Losic, D., Tiffany, M., Nagy, S. & Sterrenburg, F. The Glass Menagerie: diatoms for novel applications in nanotechnology. *Trends in Biotechnology* **27**, 116–127 (2009).
7. Li, C. *et al.* Ultrastructural and molecular characterization of diversity among small araphid diatoms all lacking rimoportulae. I. Five new genera, eight new species. *Journal of Phycology* **52**, 1018–1036 (2016).

8. Edlund, M. & Stoermer, E. Sexual reproduction in Stephanodiscus niagarae. *Journal of Phycology* **27**, 780–793 (1991).
9. Kröger, N., Lorenz, S., Brunner, E. & Sumper, M. Self-assembly of highly phosphorylated silaffins and their function in biosilica morphogenesis. *Science (New York, N.Y.)* **298**, 584–6 (2002).
10. Brunner, E. *et al*. Chitin-based organic networks: An integral part of cell wall biosilica in the diatom thalassiosira pseudonana. *Angewandte Chemie - International Edition* **48**, 9724–9727 (2009).
11. Krammer, K. & Lange-Bertalot, H. In *Süsswasser flora von Mitteleuropa* 876 (Gustav Fischer Verlag: Stuttgart, 1986).
12. Round, F., Crawford, R. & Mann, D. *The Diatoms. Biology and morphology of the genera*. (Cambridge University Press, 1990).
13. Kröger, N. & Poulsen, N. Diatoms-from cell wall biogenesis to nanotechnology. *Annual review of genetics* **42**, 83–107 (2008).
14. Ehrlich, H. & A, W. In *Biologically – Inspired* Systems (ed. Hamm, C.) 217 (Springer Science+ Business Media B. V., 2015).
15. Ehrlich, H. *et al*. Multiphase Biomineralization: Enigmatic Invasive Siliceous Diatoms Produce Crystalline Calcite. *Advanced Functional Materials*, doi:10.1002/adfm.201504891 (2016).
16. Lopez, P. J., Desclés, J., Allen, A. E. & Bowler, C. Prospects in diatom research. *Current Opinion in Biotechnology* **16**, 180–186 (2005).
17. Almqvist, N. *et al*. Micromechanical and structural properties of a pennate diatom investigated by atomic force microscopy. *Journal of Microscopy* **202**, 518–532 (2001).
18. Subhash, G., Yao, S., Bellinger, B. & Gretz, M. Diatom frustules using nanoindentation. *Journal of Nanoscience and Nanotechnology* **5**, 40–50 (2005).
19. Hamm, C. E., Merkel, R., Springer, O. & Jurkojc, P. Architecture and material properties of diatom shells provide effective mechanical protection. *Nature* **421**, 841–843 (2003).
20. Crawford, S. A., Higgins, M. J., Mulvaney, P. & Wetherbee, R. Nanostructure of the diatom frustule as revealed by atomic force and scanning electron microscopy. *Journal of Phycology* **37**, 543–554 (2001).
21. Gebeshuber, I. C. *et al*. Atomic force microscopy study of living diatoms in ambient conditions. *Journal of Microscopy* **212**, 292–299 (2003).
22. Losic, D., Short, K., Mitchell, J. & Lal, R. AFM nanoindentations of diatom biosilica surfaces. *Langmuir* **23**, 5014–5021 (2007).
23. Aw, M. S., Simovic, S., Yu, Y., Addai-Mensah, J. & Losic, D. Porous silica microshells from diatoms as biocarrier for drug delivery applications. *Powder Technology* **223**, 52–58 (2012).
24. Delalat, B. *et al*. Targeted drug delivery using genetically engineered diatom biosilica. *Nature Communications* **6**, 8791 (2015).
25. Jeffryes, C., Campbell, J., Li, H. Y., Jiao, J. & Rorrer, G. The potential of diatom nanobiotechnology for applications in solar cells, batteries, and electroluminescent devices. *Energy & Environmental Science* **4**, 3930–3941 (2011).
26. Parker, A. R. & Townley, H. E. Biomimetics of photonic nanostructures. *Nature nanotechnology* **2**, 347–353 (2007).
27. Wargo, E. A., Kotaka, T., Tabuchi, Y. & Kumbur, E. C. Comparison of focused ion beam versus nano-scale X-ray computed tomography for resolving 3-D microstructures of porous fuel cell materials. *Journal of Power Sources* **241**, 608–618 (2013).
28. Dawson, P. The morphology of the siliceous components of Didymosphaenia geminata (Lyngb.) M. Schm. *British Phycological Journal* **8**, 65–78 (1973).
29. Moffat, M. An ultrastructural study of Didymosphenia geminata (Bacillariophyceae). *Transactions of the American Microscopical Society* **113**, 59–71 (1994).
30. Spaulding, S. Didymosphenia geminata. *Diatoms of the United States*, Available at: http://westerndiatoms.colorado.edu/taxa/species/didymosphenia_geminata (2010).
31. Aboal, M., Marco, S., Chaves, E., Mulero, I. & García-Ayala, A. Ultrastructure and function of stalks of the diatom Didymosphenia geminata. *Hydrobiologia* **695**, 17–24 (2012).
32. Tkachuk, A. *et al*. X-ray computed tomography in Zernike phase contrast mode at 8 keV with 50-nm resolution using Cu rotating anode X-ray source. *Zeitschrift fur Kristallographie* **222**, 650–655 (2007).
33. Li, Q. *et al*. Pollen structure visualization using high-resolution laboratory-based hard X-ray tomography. *Biochemical and Biophysical Research Communications* **479**, 1–5 (2016).
34. Schindelin, J. *et al*. Fiji: an open source platform for biological image analysis. *Nature Methods* **9**, 676–682 (2012).

Acknowledgements

This study was supported by following research grants: the statutory funds of the Faculty of Materials Science and Engineering (Warsaw University of Technology) and the statutory funds of the University of Szczecin, Faculty of Geosciences. The authors are grateful to Dr. Matt Ashworth from the University of Texas at Austin and Prof. John P. Kociolek from the University of Colorado Boulder for critically reading the manuscript and correcting the language.

Author Contributions

I.Z. and M.P. performed the experiment and data processing of SEM/FIB; Q.L. and J.G. performed the experiment and data processing of nano-XCT; T.N. and I.Z. performed field work; I.Z. prepared the samples; I.Z., Q.L., J.G., E.Z., A.W. and K.J.K. analysed the results and co–wrote this paper; I.Z., Q.L., J.G., E.Z., A.W., R.D., R.S. and K.J.K. discussed the data; E.Z., A.W. and K.J.K. supervised the project. All authors contributed to the general discussion, revision and editing of the manuscript.

Additional Information

Competing Interests: The authors declare that they have no competing interests.

Publisher's note: Springer Nature remains neutral with regard to jurisdictional claims in published maps and institutional affiliations.

SCIENTIFIC REPORTS
nature research

OPEN

3D Diatom–Designed and Selective Laser Melting (SLM) Manufactured Metallic Structures

Izabela Zglobicka[1,2*], Agnieszka Chmielewska[3,4], Emre Topal[2,5], Kristina Kutukova[2], Jürgen Gluch[2], Peter Krüger[2], Cathy Kilroy[6], Wojciech Swieszkowski[3], Krzysztof J. Kurzydlowski[1] & Ehrenfried Zschech[2,5]

Diatom frustules, with their diverse three-dimensional regular silica structures and nano- to micrometer dimensions, represent perfect model systems for biomimetic fabrication of materials and devices. The structure of a frustule of the diatom *Didymosphenia geminata* was nondestructively visualized using nano X-ray computed tomography (XCT) and transferred into a CAD file for the first time. Subsequently, this CAD file was used as the input for an engineered object, which was manufactured by applying an additive manufacturing technique (3D Selective Laser Melting, SLM) and using titanium powder. The self-similarity of the natural and the engineered objects was verified using nano and micro XCT. The biomimetic approach described in this paper is a proof-of-concept for future developments in the scaling-up of manufacturing based on special properties of microorganisms.

Diatoms have been studied by biologists since the 18th century because of their unique, intricately patterned silica cell walls (frustules) coupled with their abundance in various aquatic and terrestrial environments. Even today, frustule shape, size, patterning and structure, observed in light and electron microscopes, are still the primary characteristics to identify diatom species[1–3]. Recently, diatoms have attracted growing attention from the engineering community since their hierarchical structure and the functionality of their frustules (which is comprised of parts or two valves) have, through the long evolution of the group, achieved levels of precision not accomplished with artificial structures manufactured by humans. Natural organisms like diatoms, which are characterized by a hierarchical architecture and a large variety of morphology, have a huge potential to be utilized as original patterns for the design of advanced materials with dedicated application-specific properties. Some applications have been described in literature (see[4–6]).

The major engineering approaches based on diatoms include:

(a) understanding and modelling of their mechanical properties[7,8];
(b) exploring the use of diatom shells in drug delivery[9,10];
(c) development of a next-generation solar cells[11,12], micro-lenses[13,14], optical sensors and biosensors[15,16];
(d) production of biofuels on a commercial scale[17];
(e) formation of nanostructured metallic micro-shells using frustules as templates[18–21].

To understand the unique properties of diatoms, their interior (hierarchical sub-structure) has been studied based on microscopic imaging of cross-sections of the shells[22,23]. Such two-dimensional (2D) visualization of biological objects is a routine task. Commonly, focused ion beam (FIB) serial cutting and subsequent scanning electron microscopy (SEM) imaging is the approach of choice for preparing and examining specimens at target sites[24]. The three-dimensional (3D) object is reconstructed from a large number of 2D images. However, the serial cutting approach has several disadvantages for the accurate representation of structures. A major drawback

[1]Faculty of Mechanical Engineering, Bialystok University of Technology, 45C Wiejska Str., 15–351, Bialystok, Poland. [2]Fraunhofer Institute for Ceramic Technologies and Systems IKTS, Maria–Reiche–Strasse 2, 01109, Dresden, Germany. [3]Faculty of Materials Science and Engineering, Warsaw University of Technology, 141 Wołoska Str., 02–507, Warsaw, Poland. [4]Materialscare LTD, 10/1 Zwierzyniecka Str., 15–333, Bialystok, Poland. [5]Dresden Center for Nanoanalysis, Dresden University of Technology, 01062, Dresden, Germany. [6]National Institute of Water & Atmospheric Research Ltd., 10 Kyle Str., Riccarton, P.O. Box 8602, Christchurch, New Zealand. *email: i.zglobicka@pb.edu.pl

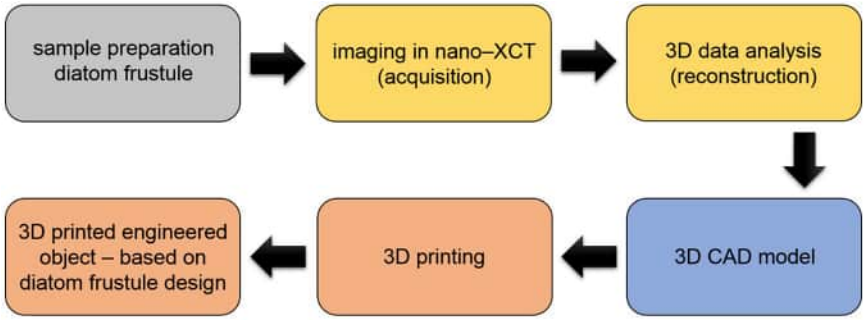

Figure 1. Flow diagram for 3D printing of an engineered object, based on the 3D nondestructive visualization of the natural object (diatom *Didymosphenia geminata*) using nano-XCT. The fabrication of the self-similar 3D object with bio-inspired design is based on accurate 3D data (CAD model).

is the generation of preparation artefacts that result in material damage caused by the interaction of the Ga^+ ion beam with the natural material. Particularly for elongated diatom species, the size of a frustule, which can be up to 5–6 mm, is too large for studying the whole 3D frustule structure using FIB/SEM serial cutting with reasonable effort. Furthermore, the excitation of electrons is increased at edges of a solid structure[25], and consequently, they generate a local high brightness in the SEM image, the so–called 'edge effect'.

In contrast to the destructive serial cutting technique, nano X–ray computed tomography (nano-XCT) provides detailed 3D information of the morphology of diatom frustules with sub-100 nm resolution[24]. Large field-of-view imaging provides an overview of the sample and allows the identification of a region of interest (ROI), and subsequent small field-of-view imaging enables the visualization of the ROI with higher resolution. Furthermore, nano-XCT at multi-keV photon energies does not require ultra-high vacuum, and therefore allows the study of diatoms at various environmental conditions.

In this paper, we describe a procedure for imaging the structure of the diatom *Didymosphenia geminata* using nano-XCT with high resolution, the generation of a CAD model and the fabrication of a self-similar, bio-inspired structure applying 3D Selective Laser Melting (SLM).

The use of several methods, including gas/solid displacement, sol-gel synthesis, polymerization and genetic/environmental manipulation, to transform biosilica into ceramics (MgO, TiO2), semi-conducting (Si-Ge) or organic scaffolds (polyaniline) structures with a retention of shape and fine features of diatom frustule structure have been reported[18,26–28]. These conversions transform the diatom frustule into a wide variety of chemistries without losing the bio-assembled 3D morphologies.

In the approach presented here, we show for the first time, an entire "work-flow" (Fig. 1) from the non-destructive depiction of the interior of a diatom frustule, through the generation of a CAD model, up to the self-similar reproduction applying additive manufacturing.

Results and Discussion

Self–similar 3D objects with bio-inspired design were fabricated using additive manufacturing based on an accurate 3D data sets (CAD model), generated based on high–resolution XCT data.

The structure of an entire frustule, with features such as ribs (purple arrowheads), and even areolae with sub-micrometer size (green rectangles), is clearly visible in the virtual cross-sections based on nano-XCT data (Fig. 2). Other visible characteristics of *D. geminata* included: stigmata (yellow stars), raphe with distal (red arrowhead) and proximal (blue arrowheads) ends (Fig. 2). Even a girdle band that was detached from the frustule is visible (Fig. 2, white arrowheads). These examples demonstrate that high-resolution and nondestructive visualization of morphology allows one to identify characteristic features of frustules of a particular diatom species, as well as variation within a group of representatives of the same species.

The radiograph in Fig. 2B shows a hole resulting from missing data of the two reconstructions that were carried out separately for headpole and footpole sections, needed because of the length of the frustule.

Because of the hierarchical architecture and the presence of specific internal substructures of diatom frustules, single radiographs are not sufficient for the visualization of their 3D internal structure. The 3D visualization of the obtained segmented data is presented in Fig. 3.

The numerical model of the sub-structure, based on a CAD model was obtained based on the reconstructed 3D data of the complete diatom frustule structure (Fig. 4). Subsequently, the data were converted into the STL file format (*.stl, STereoLitography file), which describes the external closed surfaces of the original CAD model. The *.stl file provides the basis for the calculation of slices.

For 3D printing using the SLM process, the smallest size of a single element (detail) was fixed to 100–150 µm since the particle size of the used powder was <45 µm. Considering the selected technology and the respective equipment as well as a Ti powder with a size of 45 µm, the printed structure have larger sizes than the natural diatom frustule. In this particular case, a scaling factor of 300 was used. The 3D printed object was made of pure titanium powder, i.e. not of the natural material. Despite this change, the design of the printed "diatom frustule" remained unchanged, i.e., the printed object (Fig. 5) is self-similar to the natural object (Fig. 2).

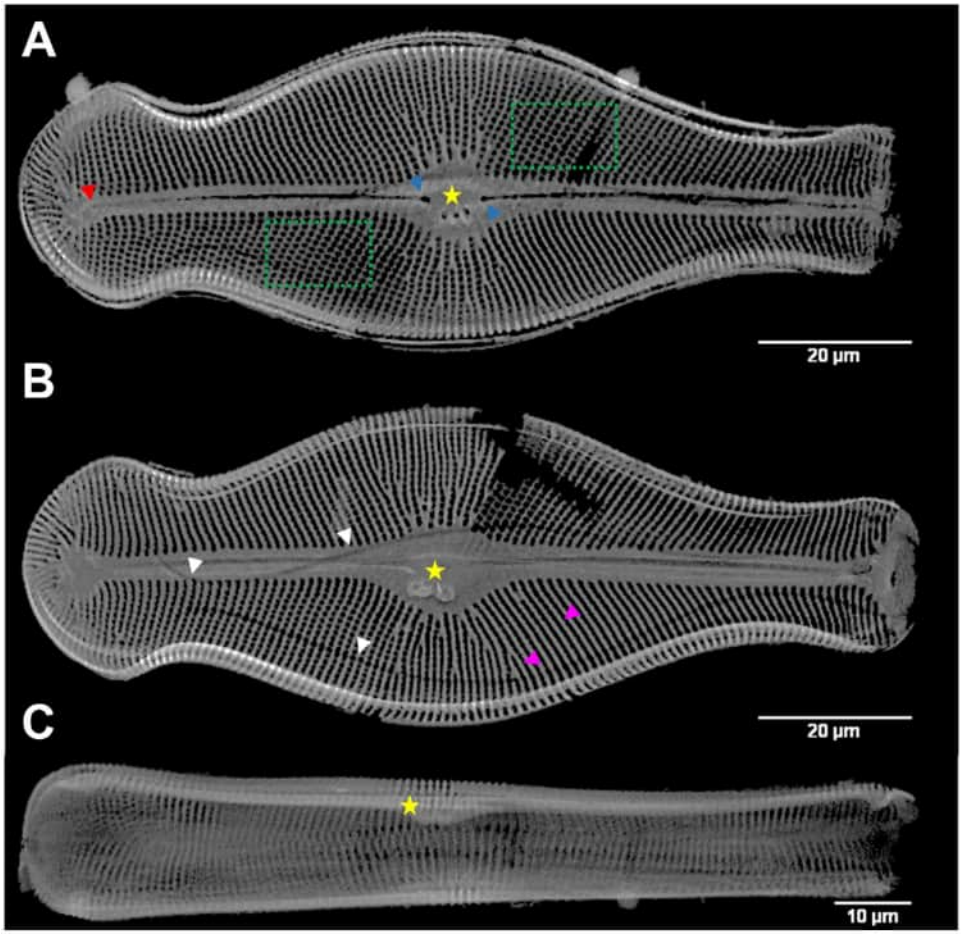

Figure 2. Nano-XCT of the frustule of *D. geminata* (in phase contrast imaging mode). (**A**–**C**) Slices extracted from the reconstructed 3D volume in (**A**) valve view – epitheca, (**B**) valve view of the interior – hypotheca, and (**C**) girdle view of the frustule. Yellow star: stigmata, red arrowhead: raphe distal end, blue arrowheads: raphe proximal ends, purple arrowheads: ribs, white arrowheads: girdle band, green rectangle: pores/areolae.

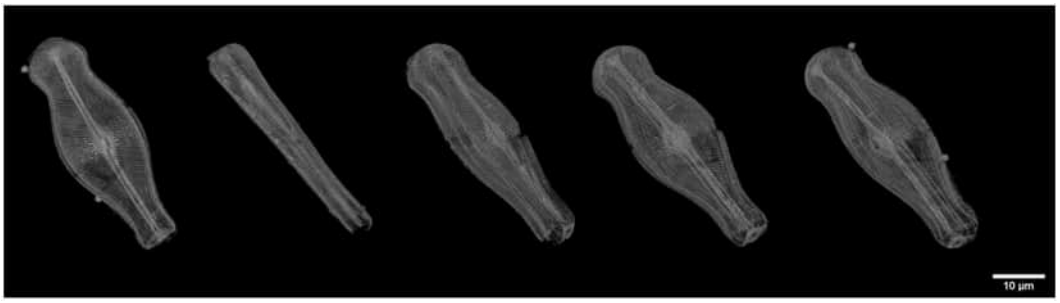

Figure 3. Three–dimensional (3D) visualization of frustule of *Didymosphenia geminata* based on nano-XCT imaging.

The macroscopic observation of the 3D printed titanium object shows a hole again (upper photo in Fig. 5) – as mentioned, resulting from missing data of the two reconstructions that were carried out separately (compare to Fig. 2).

The size of the printed object (length – ca. 3.4 cm) enables the observation of characteristic features - sub-structures of the printed object that is self-similar to the natural diatom frustule – after destructive cutting without applying microscopy (Fig. 5). However, the interior of the 3D printed self-similar object can be visualized non-destructively applying micro-XCT only (Fig. 6). Comparing the printed object (Fig. 6) with the natural diatom frustule (Fig. 2), the skeleton as well as characteristic features were preserved. Details of the diatom frustule morphology are marked in Fig. 6.

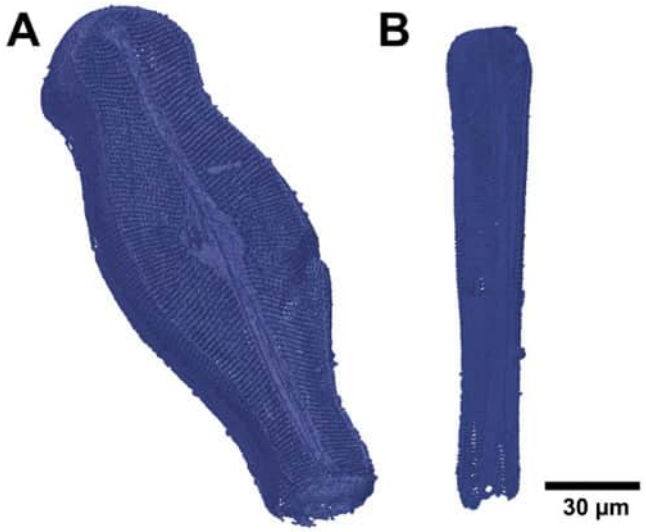

Figure 4. CAD model of *D. geminata* frustule prepared for 3D printing: (**A**) valve view, (**B**) girdle view.

Figure 5. 3D printed engineered object made of titanium, based on the natural diatom frustule design.

Both nano-XCT of the natural object and micro-XCT of the self-similar 3D-printed object allow the visualisation of the internal structures of the objects based on virtual cross-sections. As an example, two cross-sections showing ribs are compared in Fig. 7. The discontinuity between ribs, observed on a cross-section of a natural frustule, is caused by the intervals between subsequent images.

Scanning the laser point on contour allowed us to fabricate any rib of the frustule, whereas in standard hatching some of them might be omitted (due to the absence of a laser path or occurrence between paths). For the larger (wider) ribs, the empty interior is visible. The average thickness of the wall of empty ribs was determined to be 66 ± 15 µm ($n = 50$), whereas the thickness of the whole ribs in the printed object was determined to be 452 ± 129 µm ($n = 50$).

The images obtained allow a quantitative assessment (Table 1). It was possible to imitate the natural object. Note that the engineered object is about three hundred times larger than the natural diatom frustule. The SLM technique employed for this work demonstrates a high degree of reproducibility.

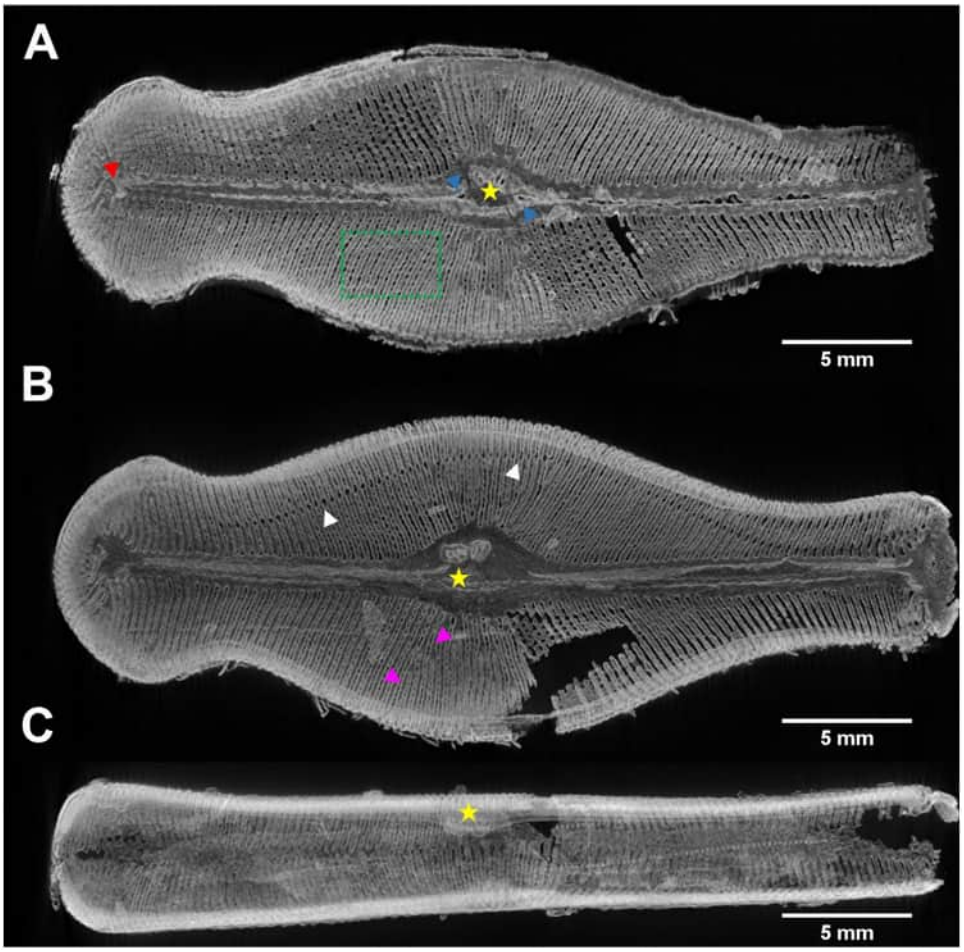

Figure 6. Micro-XCT results of the printed object based on the design of frustule of *D. geminata*. (**A**–**C**) Slices extracted from the reconstructed 3D volume in (**A**) valve view – epitheca, (**B**) valve view of the interior – hypotheca, and (**C**) girdle view of the "frustule". Yellow star: stigmata, red arrowhead: raphe distal end, blue arrowheads: raphe proximal ends, purple arrowheads: ribs, white arrowheads: girdle band, green rectangle: pores/areolae.

Conclusions

For the biomimetic approach described in this paper, a coherent workflow for the fabrication of engineered objects that are self-similar to biological objects was developed. Nano-XCT was used to determine detailed nondestructively morphological information of the diatom frustule with high spatial resolution. This diatom frustule structure was transferred into a CAD file, which was used as input for 3D printing of the up-scaled, artificial, self-similar object which was fabricated using additive manufacturing techniques, particularly SLM. The self-similarity of the natural and the engineered objects was demonstrated using X-ray computed tomography (nano-XCT for the diatom and micro-XCT for the engineered Ti object).

The size of the biological samples such as, for example, diatom frustules (length below 150 μm) make it difficult to observe characteristic features of the specimen. Our approach of combining nano-XCT with 3D printing enhances the way of visualization of the interior biological objects such as microorganisms. The enlarged engineered object allows one to visualize the sub-structures without applying a microscope, which may broaden the knowledge in fields like biology, diatom research, as well as materials science and mechanical engineering. The potential application of the diatom-based bio-inspired nanostructures include "rib-cages" which have the potential to provide mechanical protection and to constitute an innovative reinforcement component in composite materials. Furthermore, the shape and construction of openings in diatoms (i.e. pore, areolae) could be used in gas or nutrient exchange applications.

These results provide a proof-of-concept of the workflow to engineer objects that are self-similar to natural objects. Future challenges will be to determine the mechanical properties of these frustules and to optimize the properties of macroscopic size 3D structures printed using the geometrical pattern of the bio–nano–archetype.

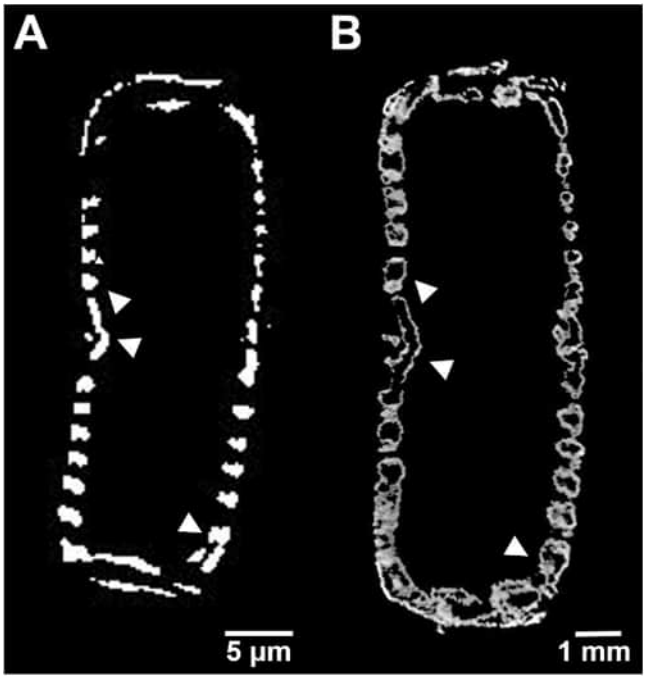

Figure 7. (**A**) Nano-XCT and (**B**) micro-XCT results of cross-sections of self-similar (**A**) natural and (**B**) printed objects based on the design of the frustule of *D. geminata* (arrowheads: ribs). Scaling up the frustule causes different scale bars.

object	length	width			
		headpole	middle	footpole	single rib
diatom frustule [µm]	116 ± 2	29 ± 1	40 ± 2	20 ± 1	0.6 ± 0.1
printed object [mm]	34 ± 1	9 ± 0	12 ± 0	6 ± 0	0.2 ± 0

Table 1. The mean values and standard deviations of sub-structures of *D. geminata*.

Experimental Materials and Methods

Materials. The *Didymosphenia geminata* samples were collected from the Upper Ohau River, South Island, New Zealand. Intact mats were carefully scraped from riverbed boulders, using a stiff plastic spatula, and gently rinsed in the flowing river water to release trapped sediment and other material. The fresh samples were drained for 2 h and dried at 37 °C for 48 h to prevent the growth of bacteria. Subsequently, the cells were separated from the stalks. The scraped and dried material was inserted into nylon-mesh filtration bags (Carl Roth GmbH, Karlsruhe, Germany) and immersed in distilled water for dialysis to remove dissolved salts from the natural stream waters. The dialyzed material was then sonicated for 12 h using a CD–4860 digital ultrasonic cleaner (Xiejian, Guangdong, China) in continuous mode without heating. The cells collected from the tube were boiled in 37% hydrogen peroxide (H_2O_2), and subsequently, in 37% hydrochloric acid (HCl) to remove organic matter and to obtain ultra–pure diatom frustules. The final suspension was washed several times with distilled water, and the clean frustules were dried in vacuum at 37 °C for 12 h.

Experimental techniques. *Nano X–ray computed tomography (nano–XCT) of diatom frustule.* A nano-XCT tool (Xradia 100, Xradia Inc., Concord/CA, USA) operated with Cu-Kα radiation was used to image the frustule of *D. geminata*[24,29]. This tool provides the resolution needed, i.e. 50 nm, to image substructures in diatoms such as the ornamentation on the frustule, including striae (rows of pores or areolae) and ribs (i.e., interstriae) separating them. Areolae of sub-micrometer size are of particular interest. While the frustule is several tens of micrometers wide, the accumulated thickness of the silica material in the frustule was estimated to be less than 10 µm.

The rotating X-ray tube of the X-ray microscope was operated at an acceleration voltage of 40 kV with a target power of about 1200 W. Since the absorption contrast in the nano-XCT images is very low for 8 keV photons, the full-field X-ray microscopy images (radiographs) were acquired in phase contrast mode[30]. An isolated and dried frustule of *D. geminata* was mounted on the top of a needle. The complete tomographic data set comprised 801 images each, which were collected for 180°, with an exposure time of 220 s per image. Gold fiducial markers were carefully positioned on the top and in the middle part of the sample for the alignment of the individual images acquired at several tilt angles for tomographic reconstruction. The images were aligned and combined using a custom plugin in ImageJ[31] and subsequently reconstructed using the Xradia Inc. commercial software package[30].

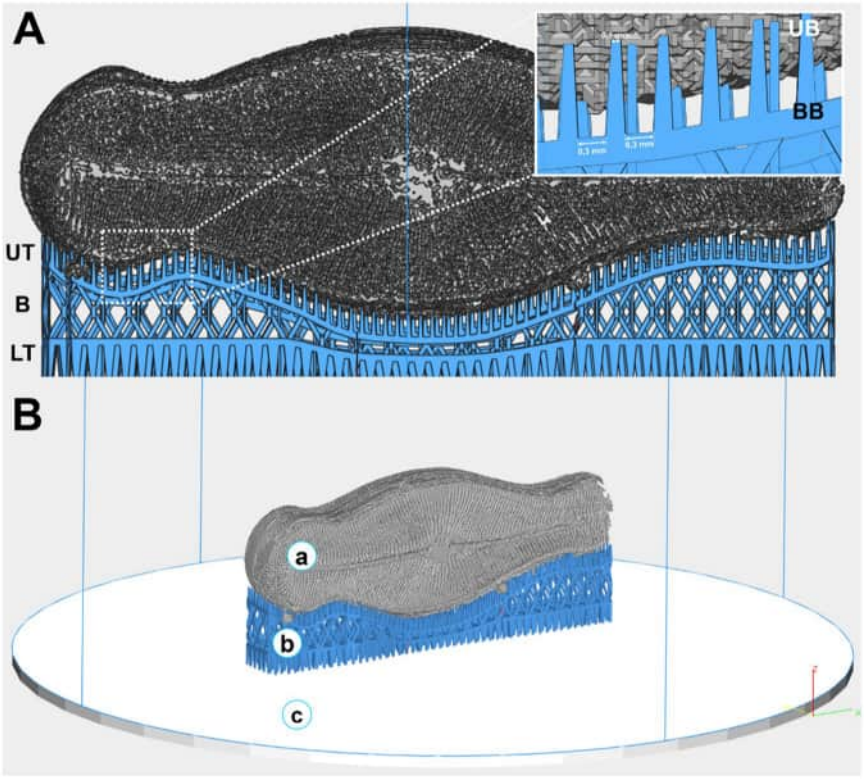

Figure 8. (**A**) Connection between the 3D printed engineered object and the support structure. UT – upper teeth, B – body, LT – lower teeth. Inset: magnification of the connection: UB – upper base, BB – bottom base. (**B**) Visualization of the 3D printed engineered object (a), support structure (b) and building platform (c).

Due to the length of the frustule (125 µm), image acquisition and reconstruction were conducted separately for the upper (headpole, or wide end) and lower (footpole, or narrow end) parts of the frustule.

3D data analysis and CAD model design. The reconstruction of a set of 2D X-ray projections (radiographs) was conducted by a filtered back projection algorithm (FBP)[32]. The reconstructed 2D image stacks - registered in ImageJ - were finally fused by stitching in order to obtain a full frustule. The final field of view was 66.5 µm with 1024 pixels, resulting in a pixel size of 65 nm. A simple threshold segmentation approach was employed to convert grey-scale images into binary images. Ultimately, the obtained 3D binary volume was transformed to a surface mesh. The quality of the surface mesh was improved using the SpaceClaim software package by closing the free edges, removing the self-intersections and making the mesh manifold in order to reduce the risk of 3D printing errors.

Printing of objects based on the diatom frustule design. The artificial objects based on the 3D design of the natural frustule were fabricated from spherical CP Ti (Grade 1) powder with a diameter smaller than 45 µm on a Realizer SLM50 desktop 3D printer (Realizer GmbH, Borchen, Germany). The processing was performed in an inert argon gas atmosphere, and the oxygen concentration was kept in the range of 0–0.2 vol %. The 3D model for the whole engineered object (based on diatom frustule design) consisted of 494 layers, each 25 µm thick. The objects that are self-similar to the frustule were 3D-printed based on the CAD model. The process parameters were determined such that a high manufacturing accuracy of the 3D structures, i.e. with a point distance of 20 µm, could be achieved. The exposure time was 20 µs, only the outer contour of each cross-section was melted. The low laser power of 17.5 W enabled melting of even small, irregular regions of the shell and ensured high manufacturing accuracy.

The support structure was designed in a way to ensure convenient detachment of the 3D object from the platform (Fig. 8A) without machining (e.g., cutting). The truss block support structure (Fig. 8A) provided the contact to the object, yet simple detachment, using 0.1 mm wide teeth spaced 0.3 mm apart. In addition, the laser power used for the support fabrication was lower than that for the object (12.5 W, compared to 17.5 W), which results in a lower strength of the support. Such an arrangement of many thin and fine teeth placed close to each other enabled the removal of the object without damage and ensured a high-quality printed object.

Chemical polishing. Post-processing steps are needed to improve the surface quality and to obtain objects with high accuracy as predicted from the CAD model. The 3D objects were manually removed from the platform and the support structures (Fig. 8B) and cleaned in an ultrasonic cleaner U-507 (Zakład Urządzeń Elektronicznych

"Ultron", Dywity/Olsztyn, Poland) using distilled water (5 times for 10 minute) to remove loose powder. Subsequently, chemical polishing in a mixture of hydrofluoric acid and nitric acid (1.25 M HF/4.5 M HNO_3) was applied for each sample using separate PTFE beakers in the ultrasonic cleaner[33]. The following chemical polishing procedure was applied:

1. Placement of the titanium object in a 20 ml PTFE beaker containing 15 ml of HF/HNO3 mixture (1 object per beaker) under sonication for 3 minutes to remove powder particles sintered to the object surfaces and to meet the targeted dimensions (from CAD model) and accuracy;
2. Removal of the acid and ultrasonic cleaning in distilled water with two solution changes, with 6 minutes sonication per water change;
3. Drying in a thermal chamber (Wamed KBC–30, Warsaw, Poland) for 2 h at 60 °C.

Computed tomography of a 3D printed self-similar object with bio-inspired design. Micro-XCT (customized tool at Fraunhofer IKTS, Dresden, Germany) was used to image the printed object. The micro-focus X-ray tube was operated at an acceleration voltage of 90 kV with a target power of about 3 W. The distance between source and detector was 1000 mm. The pixel size was 20 µm. The complete tomographic data set covering 360° was based on 1600 images, with an exposure time of 2 s for each individual image.

Received: 5 July 2019; Accepted: 9 December 2019;
Published online: 24 December 2019

References

1. Zglobicka, I. Aspects of Structural Biology of Didymosphenia geminata (Lyngb.) M. Schmidt (Bacillariophyta). *Int. J. Algae* **15**, 291–310 (2013).
2. Dabek, P. *et al*. Cymatosirella Dąbek, Witkowski & Sabbe gen. nov., a new marine benthic diatom genus (Bacillariophyta) belonging to the family Cymatosiraceae. **183**, 1–15 (2013).
3. Witkowski, A. *et al*. A Description of Biremis panamae sp. nov., a New Diatom Species from the Marine Littoral, with an Account of the Phylogenetic Position of Biremis D.G. Mann et E.J. Cox (Bacillariophyceae). *PLoS One* **9**, e114508 (2014).
4. Parker, A. R. & Townley, H. E. Biomimetics of photonic nanostructures. *Nat. Nanotechnol.* **2**, 347–353 (2007).
5. Jeffryes, C., Campbell, J., Li, H., Jiao, J. & Rorrer, G. The potential of diatom nanobiotechnology for applications in solar cells, batteries, and electroluminescent devices. *Energy Environ. Sci.* **10** (2011).
6. Delalat, B. *et al*. Targeted drug delivery using genetically engineered diatom biosilica. *Nat. Commun.* **6**, 8791 (2015).
7. Hamm, C. E. *et al*. Architecture and material properties of diatom shells provide effective mechanical protection. *Nature* **421**, 841–843 (2003).
8. Moreno, M. D., Ma, K., Schoenung, J. & Dávila, L. P. An integrated approach for probing the structure and mechanical properties of diatoms: Toward engineered nanotemplates. *Acta Biomater.* **25**, 313–324 (2015).
9. Aw, M. S., Simovic, S., Yu, Y., Addai-Mensah, J. & Losic, D. Porous silica microshells from diatoms as biocarrier for drug delivery applications. *Powder Technol.* **223**, 52–58 (2012).
10. Medarevic, D., Losic, D. & Ibric, S. Diatoms - nature materials with great potential for bioapplications. Hem. Ind. 69–69, https://doi.org/10.2298/HEMIND150708069M (2015).
11. Toster, J. *et al*. Diatom frustules as light traps enhance DSSC efficiency. *Nanoscale* **5**, 873–876 (2013).
12. Wang, C., Yu, S., Chen, W. & Sun, C. Highly efficient light-trapping structure design inspired by natural evolution. *Sci. Rep*. **3** (2013).
13. De Tommasi, E. *et al*. Biologically enabled sub-diffractive focusing. *Opt. Express* **22**, 27214 (2014).
14. De Stefano, L., Rea, I., Rendina, I., De Stefano, M. & Moretti, L. Lensless light focusing with the centric marine diatom Coscinodiscus walesii. *Opt. Express* **15**, 18082–18088 (2007).
15. De Stefano, L. *et al*. Marine diatoms as optical biosensors. *Biosens. Bioelectron.* **24**, 1580–1584 (2009).
16. Gale, D. K., Gutu, T., Jiao, J., Chang, C. H. & Rorrer, G. L. Photoluminescence detection of biomolecules by antibody-functionalized diatom biosilica. *Adv. Funct. Mater.* **19**, 926–933 (2009).
17. Wang, J. K. & Seibert, M. Prospects for commercial production of diatoms. *Biotechnol. Biofuels* **10**, 1–13 (2017).
18. Sandhage, B. K. H. *et al*. Novel, Bioclastic Route to Self-Assembled, 3D, Chemically Tailored Meso/Nanostructures: Shape-Preserving Reactive Conversion Biosilica (Diatom) Microshells. *Adv. Mater.* **14**, 429–433 (2002).
19. Payne, E. K., Rosi, N. L., Xue, C. & Mirkin, C. A. Sacrificial biological templates for the formation of nanostructured metallic microshells. *Angew. Chemie - Int. Ed.* **44**, 5064–5067 (2005).
20. Belegratis, M. R., Schmidt, V., Nees, D., Stadlober, B. & Hartmann, P. Diatom-inspired templates for 3D replication: Natural diatoms versus laser written artificial diatoms. *Bioinspiration and Biomimetics* **9**, 1–11 (2014).
21. Kwon, S., Park, S. & Nichols, W. Self-assembled Diatom Substrates with Plasmonic Functionality. *J. Korean Phys. Soc.* **64**, 1179–1184 (2014).
22. Witkowski, A. *et al*. Simonsenia aveniformis sp. nov. (Bacillariophyceae), molecular phylogeny and systematics of the genus, and a new type of canal raphe system. *Sci. Rep*. **5** (2015).
23. Bak, M. *et al*. Novel diatom species (Bacillariophyta) from the freshwater discharge site of Laguna Diablas (Island Isabela = Albemarle) from the Galapagos. **311**, 201–224 (2017).
24. Zglobicka, I. *et al*. Visualization of the internal structure of Didymosphenia geminata frustules using nano X-ray tomography. *Sci. Rep.* **7**, 1–7 (2017).
25. Wargo, E. A., Kotaka, T., Tabuchi, Y. & Kumbur, E. C. Comparison of focused ion beam versus nano-scale X-ray computed tomography for resolving 3-D microstructures of porous fuel cell materials. *J. Power Sources* **241**, 608–618 (2013).
26. Weatherspoon, M. R., Allan, S. M., Hunt, E., Cai, Y. & Sandhage, K. H. Sol-gel synthesis on self-replicating single-cell scaffolds: applying complex chemistries to nature's 3-D nanostructured templates. *Chem. Commun*. 651–653, https://doi.org/10.1039/b409466b (2005).
27. Losic, D., Mitchell, J. G. & Voelcker, N. H. Fabrication of gold nanostructures by templating from porous diatom frustules. *New J. Chem.* **30**, 908 (2006).
28. Li, X., Li, X., Dai, N. & Wang, G. Large-area fibrous network of polyaniline formed on the surface of diatomite. *Appl. Surf. Sci.* **255**, 8276–8280 (2009).
29. Zschech, E. *et al*. Laboratory Computed X-Ray Tomography – A Nondestructive Technique for 3D Microstructure Analysis of Materials. *Pract. Metallogr.* **55**, 539–555 (2018).

30. Tkachuk, A. *et al*. X-ray computed tomography in Zernike phase contrast mode at 8 keV with 50-nm resolution using Cu rotating anode X-ray source. *Zeitschrift fur Krist.* **222**, 650–655 (2007).
31. Schindelin, J. *et al*. Fiji: an open source platform for biological image analysis. *Nat. Methods* **9**, 676–682 (2012).
32. Radon, J. On the determination of functions from their integral values along certain manifolds. *IEEE Trans. Med. Imaging* **5**, 170–176 (1986).
33. Wysocki, B. *et al*. Post processing and biological evaluation of the titanium scaffolds for bone tissue engineering. *Materials (Basel)*. **9** (2016).

Acknowledgements

Izabela Zglobicka acknowledges funding provided by German Academic Exchange Service (DAAD) within Research Grants – Short–Term Grants 2017 (ID: 57314023). The authors would like to thank the NCN (National Science Center) for providing financial support to project Synthesis and characterization of novel biomaterials based on three–dimensional (3D) multifunctional titanium substrates (Grant No. 2017/25/B/ST8/01599). The authors are grateful to Prof. John P. Kociolek from the University of Colorado Boulder for critically reading the manuscript and correcting the language.

Author contributions

I.Z., K.K., E.T., P.K. and J.G. performed the experiment and data processing of nano-XCT and micro–XCT; C.K. performed field work; I.Z. prepared the samples; A. Ch. performed the experiment and data processing of 3D printing and post-processing procedure; I.Z., A. Ch., K.J.K. and E.Z. analysed the results and co-wrote this paper; I.Z., K.K., A. Ch., J.G., W.Ś., K.J.K. and E.Z. discussed the data; I.Z. and E.Z. supervised the project. All authors contributed to the general discussion, revision and editing of the manuscript.

Competing interests

The authors declare no competing interests.

Additional information

Correspondence and requests for materials should be addressed to I.Z.

Reprints and permissions information is available at www.nature.com/reprints.

Publisher's note Springer Nature remains neutral with regard to jurisdictional claims in published maps and institutional affiliations.

metals

MDPI

Article

Investigation of Energy-Absorbing Properties of a Bio-Inspired Structure

Adrian Dubicki, Izabela Zglobicka * and Krzysztof J. Kurzydłowski

Faculty of Mechanical Engineering, Bialystok University of Technology, Wiejska 45C, 15-352 Bialystok, Poland; a.dubicki@pb.edu.pl (A.D.); krzysztof.kurzydlowski@pw.edu.pl or k.kurzydlowski@pb.edu.pl (K.J.K.)
* Correspondence: i.zglobicka@pb.edu.pl

Abstract: Numerous engineering applications require lightweight structures with excellent absorption capacity. The problem of obtaining such structures may be solved by nature and especially biological structures with such properties. The paper concerns an attempt to develop a new energy-absorbing material using a biomimetic approach. The lightweight structure investigated here is mimicking geometry of diatom shells, which are known to be optimized by nature in terms of the resistance to mechanical loading. The structures mimicking frustule of diatoms, retaining the similarity with the natural shell, were 3D printed and subjected to compression tests. As required, the bio-inspired structure deformed continuously with the increase in deformation force. Finite element analysis (FEA) was carried out to gain insight into the mechanism of damage of the samples mimicking diatoms shells. The experimental results showed a good agreement with the numerical results. The results are discussed in the context of further investigations which need to be conducted as well as possible applications in the energy absorbing structures.

Keywords: bio-inspired structure; diatom frustule; compression test; energy absorption

Citation: Dubicki, A.; Zglobicka, I.; Kurzydłowski, K.J. Investigation of Energy-Absorbing Properties of a Bio-Inspired Structure. *Metals* **2021**, *11*, 881. https://doi.org/10.3390/met11060881

Academic Editors: Jürgen Eckert and Dmytro Orlov

Received: 3 April 2021
Accepted: 25 May 2021
Published: 28 May 2021

1. Introduction

Nowadays, light materials are of high interest almost in every branch of industry. Examples of extensively researched materials of light specific weight include high closed porosity foams and open porosity percolated structures. In the case of foams, the metal-based one, especially metal matrix syntactic foams (MMSFs) have become more and more important due to their desired properties (high energy absorbing and damping capability and low density) as well as numerous perspective applications (e.g., automotive) [1–6].

A relatively new research line emerging recently is focused on filling out load-bearing elements with light constructs of specific morphology—see for example [7–12]. The direction of these experiment is strictly related to their (materials and structures) energy-absorption properties.

The crushing behavior of axially loaded square aluminum extrusions with aluminum foam filler has been investigated by Hanssen et al. [7]. The parameters which were considered by Authors were: loading condition, foam density, extrusion wall strength as well as extrusion wall thickness. The experimental data were used to develop design formulas in order to predict average crush forces for both quasi-static and dynamic loading conditions. Nevertheless, also numerical prediction of the crushing behavior of aluminum foam-filled columns, can be investigated [8]. The finite element modeling developed by Santosa et al., based on available experimental data, clearly showed that crush behavior of the foam-filled column may be correctly predicted. In turn, Toksoy et al. investigated the strengthening effect of commercially available polystyrene foam as a filler for Al tubes [9]. As a result, the existence of an interaction effect which appeared as increase in average crushing load for foam filled tubes, in comparison to results of investigations of the tube and the foam, has been separately confirmed. Further experiments of the mechanisms of interaction effect between the tube and foam has been conducted by Yamada et al. [10]. The internal

structure of the foam samples during non-destructive straining was visualized using X-ray computed tomography (XCT). Obtained results showed that interaction effect between the tube and the foam essentially depended on the ratio of the mean crushing force of foam to that of the tube. Similar conclusions, that deformation of the foam-filled tubes is determined by the mean plateau force ratio of tubes to foams, have been obtained by Yang et al. [11]. Yu et al., in order to understand the effect of the foam core on the interaction and the energy absorption of foam-filled tubes, have conducted compressive tests of tubes filled with various cell sizes of Al foams [12]. Obtained results showed that deformation of the foam core is close to the overall deformation when the cell size is fine. Furthermore, the decrease in the cell size causes the increase in the interaction effect which leads to increase in the energy absorption of manufactured structures [12]. The conducted research shows that filling materials in, e.g., aluminum tubes, could effectively improve the deformation as well as absorption capacity of such structures.

The direction as well as efforts in recent studies are directed towards obtaining structures characterized by high crashworthiness and being lightweight at the same time. It seems that these two may compete between each other. However, in nature there is a wide variety of protective strategies developed by organisms which reveal complex structures with sophisticated mechanical properties [13,14]. One of the most studied structures in energy absorption applications, inspired by nature, is the honeycomb structure. Furthermore, the investigations conducted by Ha et al. (2019) showed that a bio-inspired honeycomb sandwich panel (BHSP), based on the microstructure of a woodpecker's beak, exhibits superior energy absorption capability in comparison to the conventional honeycomb sandwich panel [15]. Such properties are related to the wavy character of these structures. Authors investigated the influences of the wave amplitude, wave number as well as core thickness on the energy absorption performance of the BHSPs.

Nevertheless, several solutions based on biomimetic approach have been recently investigated. The mimicking of the coconut tree profile has been proposed by Ha et al. (2018) with the aim of enhancing the energy absorption, minimizing the initial peak crushing force as well as stabilizing the crushing process [16]. Obtained results showed that there were four modes of deformations, the initial peak force was significantly reduced and the undulation load-carrying capacity parameter was minimized. In 2020, Xiang and co-workers provide an effective guideline for designing a foam-filled energy absorber with high energy absorption efficiency mimicking the characteristics of the human skeleton [17]. The proposed structures revealed the higher energy absorption efficiency. Furthermore, the best combination of the filling, which ensures the expected results, was the increasing density of the foams from the inner to the outer tube. Except for the structure, the whole shape may also constitute a bio-inspiration of which a good example is construction of a deformation element in vehicles which absorbs energy in the case of lateral collisions based on diatom frustule (see [18]). The conducted compression tests revealed that the bio-inspired crash pads performed better than their technical counterpart. The comprehensive overview of recent advanced in the development of bio-inspired structures for energy absorption applications has been presented by Ha and Lu (2020) [19].

To obtain such a structure, the overwhelming majority of scientists are using the technique of additive manufacturing (AM), which in recent years has become a hot topic. The main advantage of AM, from which arise others, is freedom of design as well as manufacturing. In combination with the increasing accessibility of the technology, honeycombs with dual-material structures [20], structural hierarchy [21–23] and graded density [24] may be fabricated. Nevertheless, nature is rich in structures—functionally graded cellular materials worth inspiration as well due to a relatively low-density with high strength, excellent energy absorption and thermal conductivity [25].

The aim of the present paper is to demonstrate a potential use in this context of bio-inspired elements resembling the geometry of a shell of a diatom species *Didymosphenia geminata* [26,27]. Diatoms are ubiquitous microorganisms which are distinguished by unique and highly ornamented frustules (see Figure 1) made of organic silica, with a size

which ranges from 2 µm to 5.6 mm [28]. These frustules are known to exhibit a high resistance to mechanical loading—see for example [29–32]. Since organic silica as such is not considered a high strength material, one may expect that the outstanding resistance to compression of frustules stems from their intricate morphology. Thus in the current research an attempt has been made to verify the possibility of using replication of unique morphology of one of the diatom species in 3D-printed metallic counterparts ("enlarged frustule") as light-high-strength fillers. This objective was fulfilled by compression tests of the print-outs. Additionally, Finite Element analysis of the compression tests was carried out.

2. Materials and Methods

2.1. Materials

The diatom species which we used in the present case was *Didymosphenia geminata* (Figure 1). The structure of its shell was firstly nondestructively visualized using nano X-ray computed tomography (nano-XCT) and transferred into a CAD file which was used as the input for an additive manufacturing technique (3D Selective Laser Melting, SLM). The enlarged counterparts of the nano-XCT visualized frustule were fabricated using spherical CP Ti (Grade 1) powder with a diameter smaller than 45 µm employing a Realizer SLM50 desktop 3D printer (Realizar GmbH, Borchen, Germany). The entire process of obtaining an engineered object has been published in Zglobicka et al. (2019) [27]. The self-similarity of the natural and the engineered objects was demonstrated using X-ray computed tomography (nano-XCT for the diatom frustule and micro-XCT for the engineered Ti object) (see [27]). Dimensions of the printed enlarged-frustule constructs are given in Table 1.

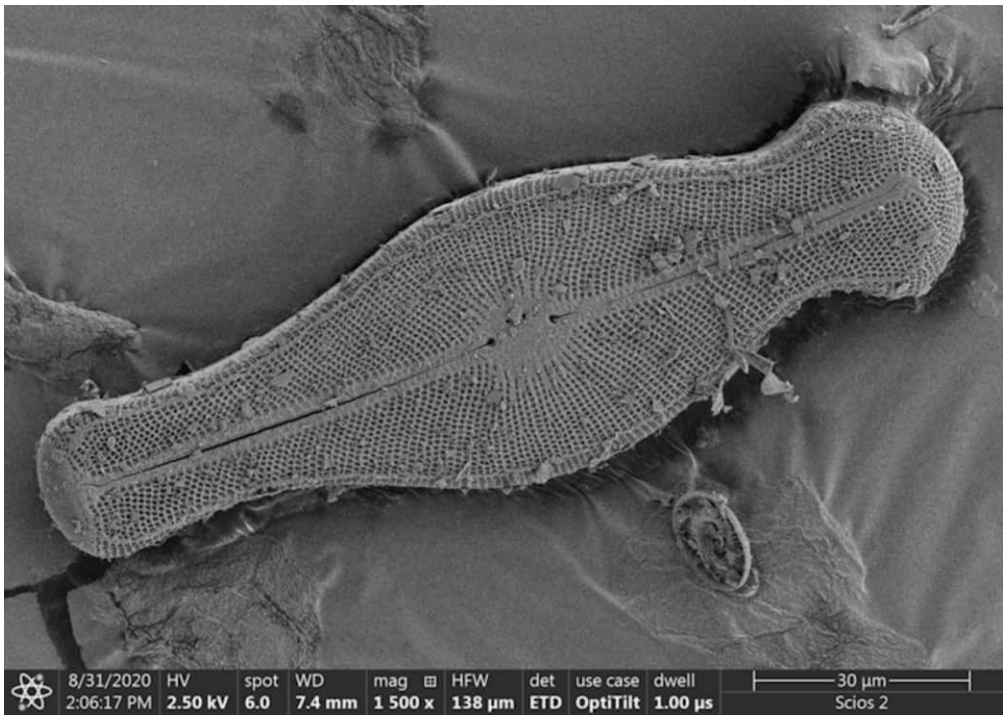

Figure 1. SEM image of *Didymosphenia geminata* (valve view).

2.2. Methods

Light Microscopy of the printed, engineered object based on the design of frustule of *D. geminata*. The printed objects were observed using a TAGARNO Prestige digital microscope (Denmark) equipped with objective lenses in the M Plan Apo 10x phase in light microscopy modus. Scanning Electron Microscopy images of the cross sections of printed frustules were obtained using an ultra-high-resolution analytical dual-beam FIB-SEM tool (Scios2 DualBeam, Thermo Fisher Scientific, Waltham, MA, USA) using acceleration voltages of 2 kV for the electrons. During observations, magnifications of 100x and 200x were used.

Compression tests of the printed, engineered object based on the design of a frustule of *D. geminata* were carried out. Experimental tests were conducted at room temperature with a test machine from MTS Insight Material Testing Systems with an axial loading range ±1 kN and stepless speed control. The applied rate of specimen displacement was l = 0.1 (mm/s).

Finite Element Analysis (FEA) of compression tests of the printed, engineered object was performed using SpaceClaim software (ANSYS Inc., Canonsburg, PA, USA). A 3D model of the ribbed surface was built based on the imported geometry, applying corrections to remove obvious imperfections of the imaging. This model was used to determine the equivalent mechanical properties of the ribbed part. In the modelling of the entire printed frustule, the ribbed part was described using equivalent mechanical properties. Simulations of the compression tests were carried out using bilinear stress–strain curves calculated based on the values for bulk Ti (Table 1).

Table 1. Values of the characteristic mechanical properties for bulk Ti and equivalent parameters for the ribbed part of the diatom frustule.

Parameter	Bulk Ti	Ribbed Part of the Diatom Frustule
Young modulus (GPa)	115	31.3
Yield point (MPa)	750	150
work hardening (MPa/1% of plastic strain)	100	28

The final mesh consisted of 42,158 finite elements. The load–displacement data obtained in compression tests were obtained assuming elastic deformation of the frustule. The main objective of the simulations was to estimate compression curve.

3. Results

Photographs of the printed samples of enlarged diatom frustule are given in Figure 2. These photographs show the valve, headpole/footpole and girdle views. Evaluation of geometry of the print-outs revealed some missing fragments of the size in the range 10 mm^2. These imperfections were regarded as non-essential and possible to avoid in future perfecting of the technology. Values of the weight, surface and volume of the printed frustules are listed in Table 2. This table lists also equivalent density of the frustules as 3D objects. This density of 0.11 g/cm^3 is by an order of a degree lower than that of standard light aluminum foams and lower that the values recently published in [33], where a value of 0.12 g/cm^3 was reported for A-242 alloy foams with over 88% porosity. It can be concluded that the printed frustule can be considered as an ultralight structure.

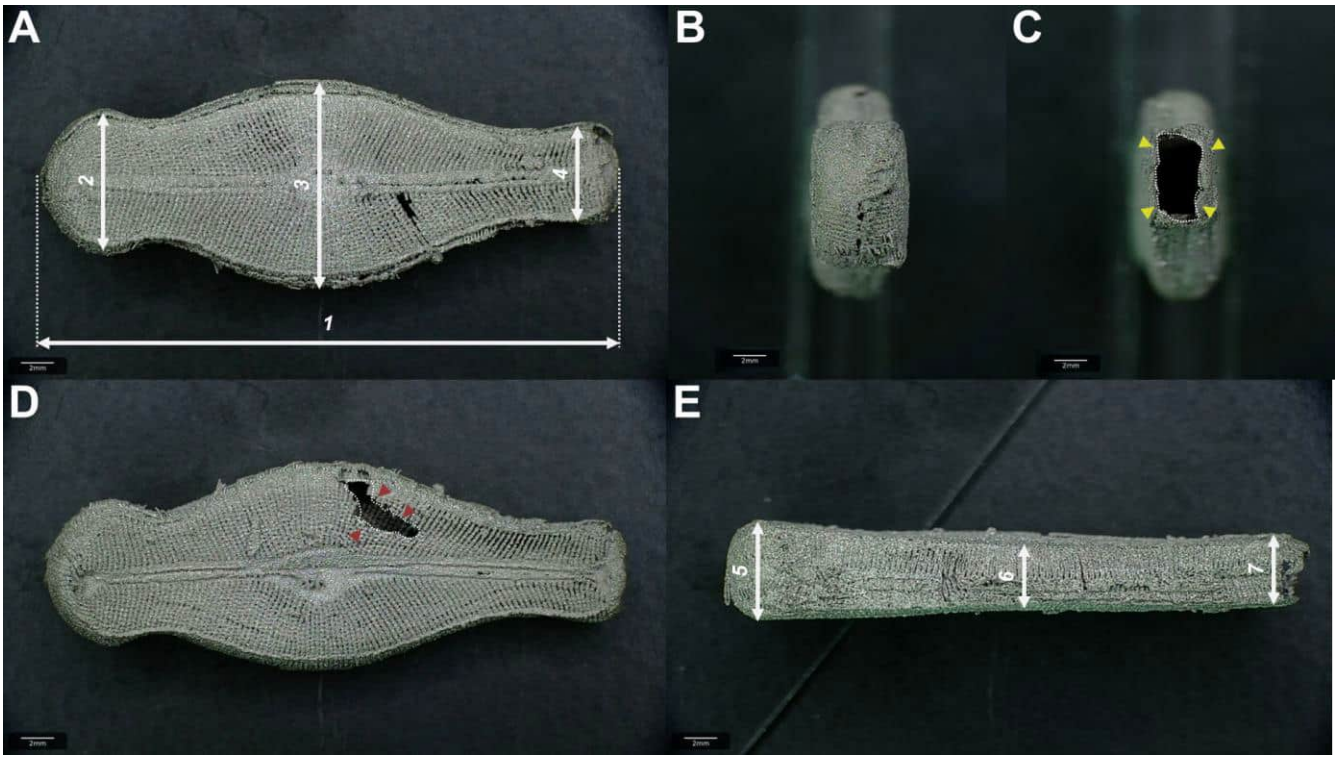

Figure 2. Photos of the printed, engineered object based on the design of frustule of *Didymosphenia geminata* before compression test: (**A**,**D**) valve view; (**B**) headpole ending; (**C**) footpole ending; (**E**) girdle band view with designations: 1—length; 2—width of the headpole, 3—width in the middle part; 4—width of the footpole; 5—thickness in the headpole; 6—thickness in the middle part; 7—thickness in the footpole.

Table 2. The weight/size characteristic of the 3D printed engineered object.

Feature	Value
weight (g)	0.866
total area (disregarding openings) (cm^2)	390.4
encompassing volume (cm^3)	7.87
equivalent density (g/cm^3)	0.11

The low density of the printed frustules stems from three factors: (a) it envelopes relatively large cavity, (b) the frustule features an intricate system of openings (struts and ribs) and (c) micro-porosity of the printed parts. The micro-porosity was revealed in the SEM investigations and is exemplified by images in Figure 3.

Characteristic dimensions of the printed frustules are provided in Table 3. This table lists values measured for as-printed frustules and for the fully flattened in compression tests.

Photos of the printed, engineered object based on the design of frustule of *Didymosphenia geminata* after compression testing are shown in Figure 4. The definitions of the respective points of measurements are explained by the arrows numbered from one to seven.

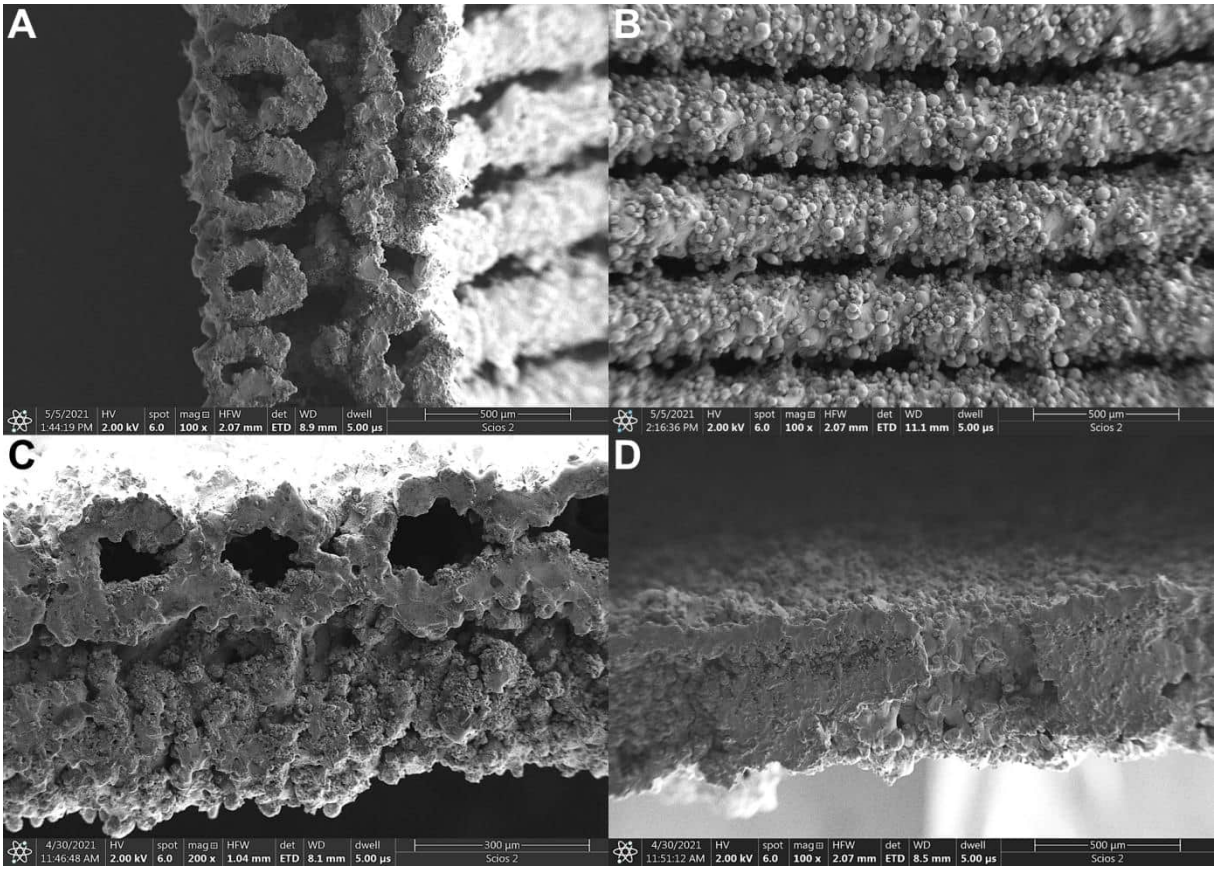

Figure 3. SEM images of the (**A**,**B**) longitudinal section and (**C**,**D**) cross-section of printed, engineered object based on the design of frustule of *Didymosphenia geminata* before compression test. Images of the (**A**) section of the ribs, (**B**) ribs from the interior view, (**C**,**D**) various construction of the wall.

Table 3. The mean values with standard deviation of the 3D printed engineered object (according to the designation in Figures 2 and 4) before and after compression testing.

View of the Frustule	Dimension	Before Compression	After Compression
valve view	Length (1) (mm)	34.90 ± 0.06	37.52 ± 0.47
	Width, head pole (2) (mm)	8.86 ± 0.04	11.99 ± 0.79
	Width, middle part (3) (mm)	12.84 ± 0.13	15.36 ± 0.69
	Width, foot pole (4) (mm)	6.11 ± 0.11	8.12 ± 0.61
girdle band view	Thickness, head pole (5) (mm)	5.91 ± 0.03	2.09 ± 0.63
	Thickness, middle part (6) (mm)	4.64 ± 0.08	2.19 ± 0.55
	Thickness, foot pole (7) (mm)	4.43 ± 0.07	2.18 ± 0.49

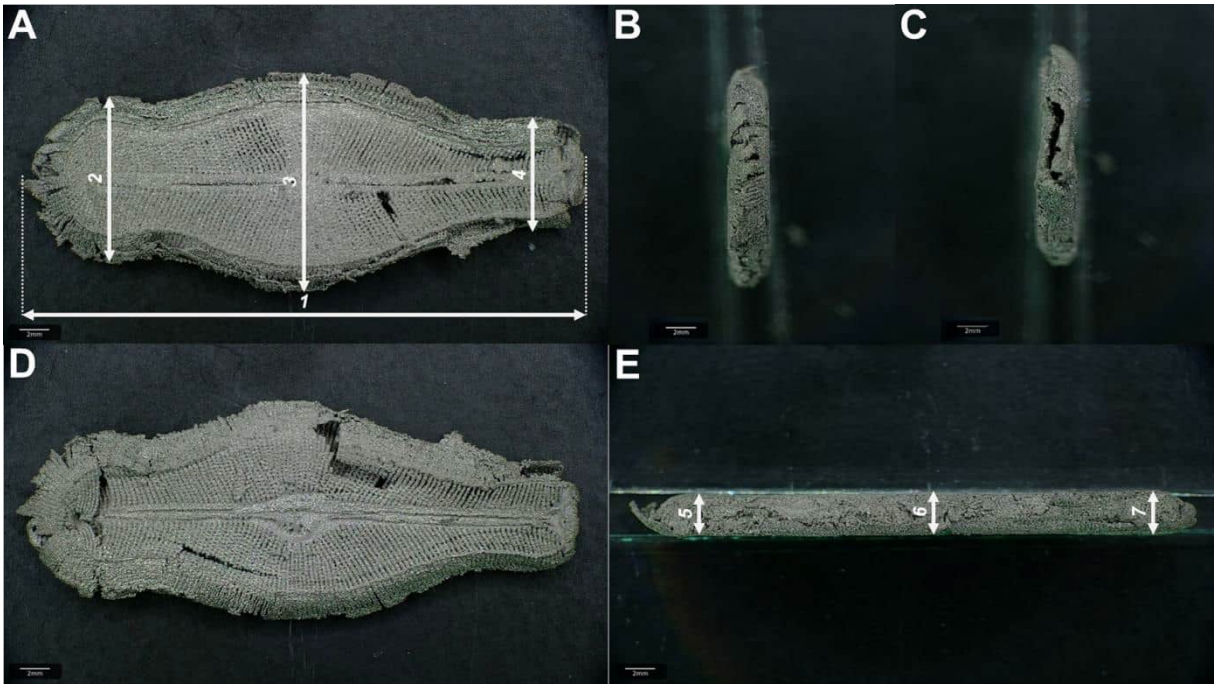

Figure 4. Photos of the printed, engineered object based on the design of frustule of *Didymosphenia geminata* after compression test: (**A**,**D**) valve view; (**B**) headpole ending; (**C**) footpole ending; (**E**) girdle band view with designations: 1—length; 2—width of the headpole, 3—width in the middle part; 4—width of the footpole; 5—thickness in the headpole; 6—thickness in the middle part; 7—thickness in the footpole.

The obtained experimental displacement–force curves are shown in Figure 5A and the respective calculated curve in Figure 5B.

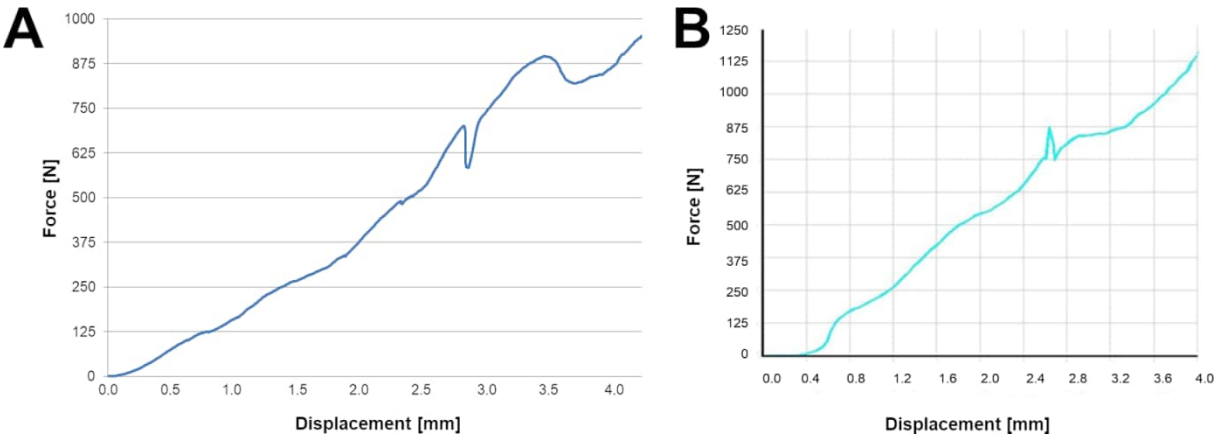

Figure 5. Force—displacement plots obtained during (**A**) experimental compression, (**B**) finite element analysis.

A remarkable agreement is observed between the two curves in Figure 5 in the entire range of displacements with the exception of compression by 2.5 mm. This amount of compression corresponds to the moment in which the bottom and upper parts of frustules come in direct contact. From that point onwards, the process of frustule densification starts, which is less precisely accounted for in the FEM simulations. The agreement for the displacements lower than 2.5 mm implies the adopted model of plastic deformation of the printed frustule under compression. In turn, it indicates that the work done by the compression force is accumulated in the compressed material via work hardening phenomena.

4. Discussion

The results presented in the paper show that a printed enlarged version of the diatom can be viewed as an ultra-light structure with a large cavity and two types of pores. Due to the concept adopted in printing, the cavity as such and the openings in the frustules have geometry optimized by the forces of nature. In the literature there are numerous reports confirming exceptional mechanical properties of diatoms and shells—see for example [29–31]. These exceptional properties protect diatoms against major predators by imparting high stiffness and resilience [30]. In the present study, we took advantage of these exceptional properties by using it as a template for printing materials with their enlarged values. As a result, tough and resilient structures were obtained, which also contained micro-porosity related to the printing process.

In view of the characteristics of the printed samples given above, generally understood energy absorption seems to an obvious area of their applications. According to the literature, the energy absorption per unit volume is higher in the graded structure in comparison to the uniform structure [34,35].

The force–displacement curves obtained in the compression test allow calculation of the mechanical work done up to the point of flattening the sample, whereas the energy absorption and energy absorption efficiency can be calculated based on the formulas [36].

$$W = \frac{1}{100}\int_0^{e_0} \sigma de \tag{1}$$

$$W_e = \frac{W}{\sigma_0 \cdot e_0} \cdot 10^4 \tag{2}$$

where

W—energy absorption per unit volume (MJ/m^3)
We—energy absorption efficiency (%)
σ—compressive stress (N/mm^2)
e_0—upper limit of the compressive strain (%)
σ_0—compressive stress at the upper limit of the compressive strain (N/mm^2)

Based on obtained results, by integrating the area underneath the curve the following value of the mechanical work was estimated: 1.90 J. With the weight of 0.866 g = 0.000866 kg and volume of 7.87 cm^3 = 0.00787 m^3, the density of the absorbed (and mostly dissipated) energy is 2194/kg and 241.4 J/m^3. These values justify further steps needed to use the present results for designing absorbing elements based on the concept adopted here. One line of such development could be filling out such components with a mixture of printed frustules of different size and orientation with expected loadings. The other could be further strengthening of the frustules by filling out their cavities with foams.

5. Conclusions

According to the literature [37], there are several mechanisms of energy absorption, which depend on the used material: elastomeric foams, plastic or brittle foams, natural, cellular materials or fluid within cells. Recent studies in energy absorption issues are mainly related to foams or thin walled tubes without or with filling in the form of various foams. Results obtained by various research groups show that the strength of the foam core affects the interaction effect. It must be noted that stress–strain curves of metal foams used in absorption applications exhibit a plateau-stress region where deformation proceeds at nearly constant nominal stress, whereas in nonporous metals stress continuously increases with the progress of deformation. The results presented in this manuscript did not allow the observation such a plateau-stress region on the plots, both experimental and theoretical. The obtained results indicate linearly decreasing resistance force and, as a consequence, the absorbed energy is half of that which would be absorbed if the force was constant (plateau region). On the other hand the specific density of the printed structure is extremely low

(equivalent density at 0.11 g/cm^3), due to the fact that the internal cavity is relatively large and empty.

The structural complexity of the porous structure of the diatom shell may be considered as an anisotropic structure. Such behavior is exhibited within so-called lotus-type porous metals, which have superior specific strength than metal foams. This is because the concentration rarely occurs around the pores when the loading is along the pore direction. It makes lotus-metals promising as functional materials with lightweight structure. Among the applications, sound absorbing, heat sinking and energy absorbing have been mentioned.

Nevertheless, the density of the 3D printed engineered object based on a diatom frustule structure is much lower than that of the same structure with the cavity filled out with any form of foam or rod-type strengthening. Thus, there is a clear space for further investigations as well as improving the structure of interest in terms of the rate of energy absorption by in-printing into the cavity a supporting scaffold.

The consideration of the energy absorption value (2.2 kJ/g) should take into account the structure features as well as void inside the frustule. This preliminary results, with an indication that derivative of the work after displacement is constant, seems to be a good introduction into further research of diatom-inspired energy absorbing structures.

The conducted investigations allowed the attainment of new as well as enrichment of the existing knowledge about behavior of the structured inspired by nature. In future work, we will further study the deformation behavior and energy absorption of bio-inspired structures in various configurations and try to predict their energy absorption capacity.

Author Contributions: Conceptualization, I.Z. and K.J.K.; methodology, A.D. and I.Z.; formal analysis, A.D., I.Z. and K.J.K.; investigation, A.D. and I.Z.; writing—original draft preparation, A.D. and I.Z.; writing—review and editing, A.D., I.Z. and K.J.K.; supervision, I.Z. and K.J.K.; project administration, I.Z.; funding acquisition, I.Z. and K.J.K. All authors have read and agreed to the published version of the manuscript.

Funding: Izabela Zgłobicka acknowledges funding provided by German Academic Exchange Service (DAAD) within Research Grants—Short—Term Grants 2017 (ID: 57314023), National Science Center for providing financial support to project Metal Matrix Composites with natural filler (Grant No. 2018/31/D/ST8/00890). Authors acknowledges funding provided withinthe program of the Minister of Science and Higher Education of Poland named “Regional Initiative of Excellence” in 2019–2022, project number 011/RID/2018/19,amount of financing 12,000,000 PLN.

Institutional Review Board Statement: Not applicable.

Informed Consent Statement: Not applicable.

Data Availability Statement: The data presented in this study are available on request from the corresponding author. The data are not publicly available due to the further ongoing experiments.

Acknowledgments: The authors are grateful to Kamil Pyszniak and Wojciech Grodzki for support in carrying out modeling as well as compression test.

Conflicts of Interest: The authors declare no conflict of interest.

References

1. Orbulov, I.N.; Dobránszky, J. Producing metal matrix syntactic foams by pressure infiltration. *Period. Polytech. Mech. Eng.* **2008**, *52*, 35–42. [CrossRef]
2. Orbulov, I.N.; Ginsztler, J. Compressive behaviour of metal matrix syntactic foams. *Acta Polytech. Hung.* **2012**, *9*, 43–56.
3. Orbulov, I.N.; Májlinger, K. Description of the compressive response of metal matrix syntactic foams. *Mater. Des.* **2013**, *49*, 1–9. [CrossRef]
4. Movahedi, N.; Murch, G.E.; Belova, I.V.; Fiedler, T. Functionally graded metal syntactic foam: Fabrication and mechanical properties. *Mater. Des.* **2019**, *168*, 107652. [CrossRef]
5. Movahedi, N.; Murch, G.E.; Belova, I.V.; Fiedler, T. Manufacturing and compressive properties of tube-filled metal syntactic foams. *J. Alloys Compd.* **2020**, *822*, 153465. [CrossRef]
6. Orbulov, I.N.; Szlancsik, A.; Kemény, A.; Kincses, D. Compressive mechanical properties of low-cost, aluminium matrix syntactic foams. *Compos. Part A Appl. Sci. Manuf.* **2020**, *135*, 105923. [CrossRef]

7. Hanssen, A.G.; Langseth, M.; Hopperstad, O.S. Static and dynamic crushing of square aluminum extrusions with aluminum foam filler. *Int. J. Impact Eng.* **2000**, *24*, 347–383. [CrossRef]
8. Santosa, S.P.; Wierzbicki, T.; Hanssen, A.G.; Langseth, M. Experimental and numerical studies of foam-filled sections. *Int. J. Impact Eng.* **2000**, *24*, 509–534. [CrossRef]
9. Toksoy, A.K.; Güden, M. The strengthening effect of polystyrene foam filling in aluminum thin-walled cylindrical tubes. *Thin-Walled Struct.* **2005**, *43*, 333–350. [CrossRef]
10. Yamada, Y.; Banno, T.; Xie, Z.; Wen, C. Energy absorption and crushing behaviour of foam-filled aluminium tubes. *Mater. Trans.* **2005**, *46*, 2633–2636. [CrossRef]
11. Yang, X.; An, T.; Wu, Z.; Zou, T.; Song, H.; Sha, J.; He, C.; Zhao, N. The effect of outer tube on quasi-static compression behavior of aluminum foam-filled tubes. *Compos. Struct.* **2020**, *245*, 112357. [CrossRef]
12. Yu, Y.; Cao, Z.; Tu, G.; Mu, Y. Energy absorption of different cell structures for closed-cell foam-filled tubes subject to uniaxial compression. *Metals* **2020**, *10*, 1579. [CrossRef]
13. Naleway, S.E.; Porter, M.M.; McKittrick, J.; Meyers, M.A. Structural Design Elements in Biological Materials: Application to Bioinspiration. *Adv. Mater.* **2015**, *27*, 5455–5476. [CrossRef] [PubMed]
14. Naleway, S.E.; Taylor, J.R.A.; Porter, M.M.; Meyers, M.A.; McKittrick, J. Structure and mechanical properties of selected protective systems in marine organisms. *Mater. Sci. Eng. C* **2016**, *59*, 1143–1167. [CrossRef] [PubMed]
15. Ha, N.S.; Lu, G.; Xiang, X. Energy absorption of a bio-inspired honeycomb sandwich panel. *J. Mater. Sci.* **2019**, *54*, 6286–6300. [CrossRef]
16. Ha, N.S.; Lu, G.; Xiang, X. High energy absorption efficiency of thin-walled conical corrugation tubes mimicking coconut tree configuration. *Int. J. Mech. Sci.* **2018**, *148*, 409–421. [CrossRef]
17. Xiang, X.; Zou, S.; Ha, N.S.; Lu, G.; Kong, I. Energy absorption of bio-inspired multi-layered graded foam-filled structures under axial crushing. *Compos. Part B Eng.* **2020**, *198*, 108216. [CrossRef]
18. Hundertmark, C.; Tinter, R.; Ortelt, M.; Hauser, M.J.B. Diatom-inspired Plastic Deformation Elements for Energy Absorption in Automobiles. *J. Bionic Eng.* **2015**, *12*, 613–623. [CrossRef]
19. Ha, N.S.; Lu, G. A review of recent research on bio-inspired structures and materials for energy absorption applications. *Compos. Part B Eng.* **2020**, *181*, 107496. [CrossRef]
20. Wang, K.; Chang, Y.H.; Chen, Y.W.; Zhang, C.; Wang, B. Designable dual-material auxetic metamaterials using three-dimensional printing. *Mater. Des.* **2015**, *67*, 159–164. [CrossRef]
21. Ajdari, A.; Jahromi, B.H.; Papadopoulos, J.; Nayeb-Hashemi, H.; Vaziri, A. Hierarchical honeycombs with tailorable properties. *Int. J. Solids Struct.* **2012**, *49*, 1413–1419. [CrossRef]
22. Oftadeh, R.; Haghpanah, B.; Vella, D.; Boudaoud, A.; Vaziri, A. Optimal fractal-like hierarchical honeycombs. *Phys. Rev. Lett.* **2014**, *113*, 1–5. [CrossRef]
23. Brennan-Craddock, J.; Brackett, D.; Wildman, R.; Hague, R. The design of impact absorbing structures for additive manufacture. *J. Phys. Conf. Ser.* **2012**, *382*. [CrossRef]
24. Maskery, I.; Hussey, A.; Panesar, A.; Aremu, A.; Tuck, C.; Ashcroft, I.; Hague, R. An investigation into reinforced and functionally graded lattice structures. *J. Cell. Plast.* **2017**, *53*, 151–165. [CrossRef]
25. Schaedler, T.A.; Carter, W.B. Architected Cellular Materials. *Annu. Rev. Mater. Res.* **2016**, *46*, 187–210. [CrossRef]
26. Zglobicka, I.; Li, Q.; Gluch, J.; Płocińska, M.; Noga, T.; Dobosz, R.; Szoszkiewicz, R.; Witkowski, A.; Zschech, E.; Kurzydłowski, K.J. Visualization of the internal structure of Didymosphenia geminata frustules using nano X-ray tomography. *Sci. Rep.* **2017**, *7*, 1–7. [CrossRef]
27. Zglobicka, I.; Chmielewska, A.; Topal, E.; Kutukova, K.; Gluch, J.; Krüger, P.; Kilroy, C.; Swieszkowski, W.; Kurzydlowski, K.J.; Zschech, E. 3D Diatom–Designed and Selective Laser Melting (SLM) Manufactured Metallic Structures. *Sci. Rep.* **2019**, *9*, 1–9. [CrossRef]
28. Round, F.; Crawford, R.; Mann, D. *The Diatoms. Biology and Morphology of the Genera*; Cambridge University Press: Cambridge, UK, 1991.
29. Almqvist, N.; Delamo, Y.; Smith, B.L.; Thomson, N.H.; Bartholdson, Å.; Lal, R.; Brzezinski, M.; Hansma, P.K. Micromechanical and structural properties of a pennate diatom investigated by atomic force microscopy. *J. Microsc.* **2001**, *202*, 518–532. [CrossRef]
30. Hamm, C.E.; Merkel, R.; Springer, O.; Jurkojc, P.; Maiert, C.; Prechtelt, K.; Smetacek, V. Architecture and material properties of diatom shells provide effective mechanical protection. *Nature* **2003**, *421*, 841–843. [CrossRef]
31. Subhash, G.; Yao, S.; Bellinger, B.; Gretz, M.R. Investigation of mechanical properties of diatom frustules using nanoindentation. *J. Nanosci. Nanotechnol.* **2005**, *5*, 50–56. [CrossRef] [PubMed]
32. Topal, E.; Rajendran, H.; Zgłobicka, I.; Gluch, J.; Liao, Z.; Clausner, A.; Kurzydłowski, K.J.; Zschech, E. Numerical and experimental study of the mechanical response of diatom frustules. *Nanomaterials* **2020**, *10*, 959. [CrossRef]
33. Rivera, N.M.T.; Torres, J.T.; Valdés, A.F. A-242 aluminium alloy foams manufacture from the recycling of beverage cans. *Metals* **2019**, *9*, 92. [CrossRef]
34. Li, D.; Liao, W.; Dai, N.; Xie, Y.M. Comparison of Mechanical Properties and Energy Absorption of Sheet-Based and Strut-Based Gyroid Cellular Structures with Graded Densities. *Materials* **2019**, *12*, 2183. [CrossRef]
35. Li, S.; Zhao, S.; Hou, W.; Teng, C.; Hao, Y.; Li, Y.; Yang, R.; Misra, R.D.K. Functionally Graded Ti-6Al-4V Meshes with High Strength and Energy Absorption. *Adv. Eng. Mater.* **2016**, *18*, 34–38. [CrossRef]